# The SARS-CoV-2 conserved macrodomain is a highly efficient ADP-ribosylhydrolase

Yousef M.O. Alhammad[a], Maithri M. Kashipathy[b], Anuradha Roy[c], Jean-Philippe Gagné[d,e], Louis Nonfoux[d,e], Peter McDonald[c], Philip Gao[f], Kevin P. Battaile[g], David K. Johnson[h], Guy G. Poirier[d,e], Scott Lovell[b] and Anthony R. Fehr[a,#]

[a]Department of Molecular Biosciences, University of Kansas, Lawrence, Kansas 66045, USA
[b]Protein Structure Laboratory, University of Kansas, Lawrence, Kansas 66047, USA
[c]High Throughput Screening Laboratory, University of Kansas, Lawrence, Kansas 66047, USA
[d]Department of Molecular Biology, Medical Biochemistry and Pathology, Laval University Cancer Research Center, Québec City, QC, G1V 0A6, Canada
[e]CHU de Québec Research Center, CHUL Pavilion, Oncology Division, Québec City, QC, G1V 4G2, Canada
[f]Protein Production Group, University of Kansas, Lawrence, Kansas 66047, USA
[g]NYX, New York Structural Biology Center, Upton, NY 11973, USA
[h]Molecular Graphics and Modeling Laboratory and the Computational Chemical Biology Core, University of Kansas, Lawrence, Kansas 66047, USA

[#]Correspondence: arfehr@ku.edu; Tel.: +1- (785) 864-6626 (K.S.)

Running title: SARS-CoV-2 Mac1 removes ADP-ribose from protein

Keywords: Coronavirus, SARS-CoV-2, macrodomain, ADP-ribose, poly-ADP-ribose,

**ABSTRACT**

Severe acute respiratory syndrome coronavirus 2 (SARS-CoV-2) and other SARS-like-CoVs encode 3 tandem macrodomains within non-structural protein 3 (nsp3). The first macrodomain, Mac1, is conserved throughout CoVs, binds to and hydrolyzes mono-ADP-ribose (MAR) from target proteins. Mac1 likely counters host-mediated anti-viral ADP-ribosylation, a posttranslational modification that is part of the host response to viral infections. Mac1 is essential for pathogenesis in multiple animal models of CoV infection, implicating it as a virulence factor and potential therapeutic target. Here we report the crystal structure of SARS-CoV-2 Mac1 in complex with ADP-ribose. SARS-CoV-2, SARS-CoV and MERS-CoV Mac1 exhibit similar structural folds and all 3 proteins bound to ADP-ribose with low μM affinities. In contrast, we found that only the MERS-CoV Mac1 protein bound to poly-ADP-ribose (PAR), and none of these enzymes could hydrolyze PAR. Importantly, using ADP-ribose detecting antibodies and both gel-based assay and novel ELISA assays, we demonstrated highly efficient de-MARylating activity for all 3 CoV Mac1 proteins. We conclude that the SARS-CoV-2 and other CoV Mac1 proteins are highly efficient MAR-hydrolases with strikingly similar activity, indicating that compounds targeting CoV Mac1 proteins may have broad anti-CoV activity.

40 **IMPORTANCE**

41 SARS-CoV-2 has recently emerged into the human population and has led to a worldwide
42 pandemic of COVID-19 that has caused nearly 350 thousand deaths worldwide. With, no
43 currently approved treatments, novel therapeutic strategies are desperately needed. All
44 coronaviruses encode for a highly conserved macrodomain (Mac1) that binds to and removes
45 ADP-ribose adducts from proteins in a dynamic post-translational process increasingly
46 recognized as an important factor that regulates viral infection. The macrodomain is essential for
47 CoV pathogenesis and may be a novel therapeutic target. Thus, understanding its biochemistry
48 and enzyme activity are critical first steps for these efforts. Here we report the crystal structure of
49 SARS-CoV-2 Mac1 in complex with ADP-ribose, and describe its ADP-ribose binding and
50 hydrolysis activities in direct comparison to SARS-CoV and MERS-CoV Mac1 proteins. These
51 results are an important first step for the design and testing of potential therapies targeting this
52 unique protein domain.

53

54 **INTRODUCTION**

55 The recently emerged pandemic outbreak of COVID-19 is caused by a novel coronavirus
56 named severe acute respiratory syndrome coronavirus 2 (SARS-CoV-2) (1, 2). As of May 28,
57 2020, this virus has been responsible for ~ 5.7 million cases of COVID-19 and >350,000 deaths
58 worldwide. SARS-CoV-2 is a member of the lineage B β-CoVs with overall high sequence
59 similarity with other SARS-like CoVs, including SARS-CoV. While most of the genome is
60 >80% similar with SARS-CoV, there are regions where amino acid conservation is significantly
61 lower. As expected, the most divergent proteins in the SARS-CoV-2 genome from SARS-CoV
62 include the Spike glycoprotein and several accessory proteins including 8a (absent), 8b
63 (extended), and 3b (truncated). However, somewhat unexpectedly, several non-structural
64 proteins also show significant divergence from SARS-CoV, including non-structural proteins 3,
65 4, and 7, which could affect the biology of SARS-CoV-2 (3, 4).

66 Coronaviruses encode 16 non-structural proteins that are translated from two open
67 reading frames (ORFs), replicase 1a and 1ab (rep1a and rep1ab) (5). The largest non-structural
68 protein is the non-structural protein 3 (nsp3) that encodes for multiple modular protein domains.
69 These domains in SARS-CoV-2 diverge in amino acid sequence from SARS-CoV as much as
70 30%, and SARS-CoV-2 nsp3 includes a large insertion of 25-41 residues just upstream of the
71 first of three tandem macrodomains (Mac1, Mac2, and Mac3) (Fig. 1A) (3). In addition to this
72 insertion, the individual macrodomains show large amounts of amino acid divergence. Mac1
73 diverges 28% from SARS-CoV and 59% from MERS-CoV, while Mac2 and Mac3 diverge 24%
74 from SARS-CoV. It is feasible that these significant sequence differences could impact the
75 unique biology of SARS-CoV-2. However, macrodomains have a highly conserved structure,
76 and thus sequence divergence may have little impact on their overall function. Mac1 is present in

77 all CoVs, unlike Mac2 and Mac3, and early structural and biochemical data demonstrated that it
78 contains a conserved three-layered α/β/α fold and binds to mono-ADP-ribose (MAR), poly-ADP-
79 ribose (PAR), and other related molecules (6-10). ADP-ribose is buried in a hydrophobic cleft
80 where the ADP-ribose binds to several highly-conserved residues such as aspartic acid at
81 position 23 (D23) and asparagine at position 41 (N41) of SARS-CoV (6). Mac1 homologs are
82 also found in alphaviruses, Hepatitis E virus, and Rubella virus, and structural analysis of these
83 macrodomains have demonstrated that they are very similar to CoV Mac1 (11, 12). All are
84 members of the larger MacroD-type macrodomain family, which includes human macrodomains
85 Mdo1 and Mdo2 (13).

86 The CoV Mac1 was originally named ADP-ribose-1”-phosphatase (ADRP) based on data
87 demonstrating that it could remove the phosphate group from ADP-ribose-1”-phosphate (6-8).
88 However, the activity was rather modest, and it was unclear why this would impact a virus
89 infection. More recently it has been demonstrated that CoV Mac1 can hydrolyze the bond
90 between amino acid chains and ADP-ribose molecules (14-16), indicating that it can reverse
91 protein ADP-ribosylation (6, 8). ADP-ribosylation is a post-translational modification catalyzed
92 by ADP-ribosyltransferases (ARTs, also known as PARPs) through transferring an ADP-ribose
93 moiety from $NAD^+$ onto target proteins (17). The ADP-ribose is transferred as a single units of
94 MAR, or single units of MAR are transferred consecutively to form a PAR chain. CoV Mac1
95 proteins hydrolyze MAR, but have minimal activity against PAR (14, 15). Several MARylating
96 PARPs are induced by interferon (IFN) and are known to inhibit virus replication, implicating
97 MARylation in the host-response to infection (18).

98 Several reports have addressed the role of Mac1 on the replication and pathogenesis of
99 CoVs, mostly using the mutation of a highly conserved asparagine to alanine. This mutation

100 abolished the MAR-hydrolase activity of SARS-CoV Mac1 (16). This mutation has minimal
101 effects on CoV replication in transformed cells, but reduces viral load, leads to enhanced IFN
102 production, and strongly attenuates both Murine Hepatitis Virus (MHV) and SARS-CoV in
103 mouse models of infection (7, 16, 19, 20). MHV Mac1 was also required for efficient replication
104 in primary macrophages, which could be partially rescued by the PARP inhibitors XAV-939 and
105 3-AB or siRNA knockdown of PARP12 or PARP14 (21). These data suggest that Mac1's likely
106 function is to counter PARP-mediated anti-viral ADP-ribosylation (22). Mutations in the
107 alphavirus and HEV macrodomain also have substantial phenotypic effects on virus replication
108 and pathogenesis (14, 23-26). As viral macrodomains are clearly important virulence factors,
109 they are considered to be potential targets for anti-viral therapeutics (22).
110 Based on the close structural similarities between viral macrodomains, we hypothesized
111 that SARS-CoV-2 Mac1 has similar binding and hydrolysis activity as other CoV Mac1
112 enzymes. In this study, we determined the crystal structure of the SARS-CoV-2 Mac1 protein
113 bound to ADP-ribose. Binding to MAR and PAR was tested and directly compared to a human
114 macrodomain (Mdo2) and the SARS-CoV and MERS-CoV Mac1 proteins by several *in vitro*
115 assays. All CoV Mac1 proteins bound to MAR with similar affinity, but only the MERS-CoV
116 Mac1 could bind to PAR. Finally, we demonstrated that SARS-CoV-2, SARS-CoV, and MERS-
117 CoV Mac1 proteins could efficiently remove MAR from a protein substrate, but did not remove
118 PAR. These results indicate very similar function for CoV Mac1 proteins, and will be
119 instrumental in the design and testing of novel therapeutic agents targeting the CoV Mac1
120 protein domain.
121

122 **RESULTS**

123 **Structure of the SARS-CoV-2 Mac1 complexed with ADP-ribose.** To create recombinant
124 SARS-CoV-2 Mac1 for structure determination and enzyme assays, nucleotides 3348-3872 of
125 SARS-CoV-2 isolate Wuhan-hu-1 (accession number NC_045512), representing amino acids
126 I1023-K1197 of rep1a, were cloned into a bacterial expression vector containing an N-terminal
127 6X-His tag and TEV cleavage site. We obtained large amounts (>100 mg) of purified
128 recombinant protein (Fig. S1A). A small amount of this protein was digested by the TEV
129 protease to obtain protein devoid of any extra tags for crystallization and used to obtain crystals
130 from which the structure was determined (Fig. S1B). Our crystallization experiments resulted in
131 the same crystal form (needle clusters) from several conditions, but only when ADP-ribose was
132 added to the protein. This represents an additional crystal form ($P2_1$) amongst the recently
133 determined SARS-CoV-2 macrodomain structures (27-29).

134 The structure of SARS-CoV-2 Mac1 complexed with ADP-ribose was obtained using X-
135 ray diffraction data to 2.2 Å resolution and contained four molecules in the asymmetric unit that
136 were nearly identical. The polypeptide chains could be traced from V3-M171 for subunits A/C
137 and V3-K172 for subunits B/D. Superposition of subunits B-D onto subunit A (169 residues
138 aligned) yielded RMSD deviations of 0.17 Å, 0.17 Å and 0.18 Å respectively between Cα atoms.
139 As such, subunit A was used for the majority of the structure analysis described herein. The
140 SARS-CoV-2 Mac1 protein adopted a fold consistent with the MacroD subfamily of
141 macrodomains that contains a core composed of a mixed arrangement of 7 β-sheets (parallel and
142 antiparallel) that are flanked by 6 α-helices (Fig. 2A-B).

143 As mentioned above, apo crystals were never observed for our construct, though the apo
144 structure has been solved by researchers at The Center for Structural Genomics of Infectious

145 Diseases (PDB 6WEN) (28) and the University of Wisconsin-Milwaukee (PDB 6WEY) (27).
146 Further analysis of the amino acid sequences used for expression and purification revealed that
147 our construct had 5 additional residues at the C-terminus (MKSEK) and differs slightly at the N-
148 terminus as well (GIE vs GE) relative to 6WEN. In addition, the sequence used to obtain the
149 structure of 6WEY is slightly shorter than SARS-CoV-2 Mac1 at both the N and C-terminal
150 regions (Fig. S2A). To assess the effect of these additional residues on crystallization, chain B
151 of the SARS-CoV-2 Mac1, which was traced to residue K172, was superimposed onto subunit A
152 of PDB 6W02 (29), a previously determined structure of ADP-ribose bound SARS-CoV-2 Mac1.
153 Analysis of the crystal packing of 6W02 indicates that the additional residues at the C-terminus
154 would clash with symmetry related molecules (Fig. S2B). This suggests that the presence of
155 these extra residues at the C-terminus likely prevented the generation of the more tightly packed
156 crystal forms obtained for 6W02 and 6WEY, which diffracted to high resolution.
157 The ADP-ribose binding pocket contained large regions of positive electron density
158 consistent with ADP-ribose molecules (Fig. 3A). The adenine forms two hydrogen bonds with
159 D22-I23, which makes up a small loop between β2 and the N-terminal half of α1. The side chain
160 of D22 interacts with N6, while the backbone nitrogen atom of I23 interacts with N1, in a very
161 similar fashion to the SARS-CoV macrodomain (6). A large number of contacts are made in the
162 loop between β3 and α2 which includes many highly-conserved residues, including a GGG
163 (motif) and N40, which is completely conserved in all enzymatically active macrodomains (30).
164 N40 is positioned to make hydrogen bonds with the 3' OH groups of the distal ribose, as well as
165 a conserved water molecule. K44 and G46 also make hydrogen bonds with the 2' OH of the
166 distal ribose, G48 makes contact with the 1' OH and a water that resides near the catalytic site,
167 while the backbone nitrogen atom of V49 hydrogen bonds with the α-phosphate. The other major

168 interactions with ADP-ribose occur in residues G130, I131, and F132 that are in the loop
169 between β6 and α5 (Fig. 3B). The α-phosphate accepts a hydrogen bond from the nitrogen atom
170 of I131, while the β-phosphate accepts hydrogen bonds from the backbone nitrogen atom of
171 G130 and F132. Loops β3-α2 and β6-α5 are connected by an isoleucine bridge that forms a
172 narrow channel around the diphosphate which helps position the terminal ribose for water-
173 mediated catalysis (6). Additionally, a network of direct contacts of ADP-ribose to solvent along
174 with water mediated contacts to the protein are shown (Fig. 3C).

175 **Comparison of SARS-CoV-2 Mac1 with other CoV macrodomain structures.** We
176 next sought to compare the SARS-CoV-2 Mac1 to other deposited structures of this protein.
177 Superposition with Apo (6WEN) and ADP-ribose complexed protein (6W02) yielded RMSD of
178 0.48 Å (168 residues) and 0.37 Å (165 residues), respectively, indicating a high degree of
179 similarity (Fig. S3A-B). Comparison of the ADP-ribose binding site of SARS-CoV-2 Mac1 with
180 that of the apo structure (6WEN) revealed minor conformational differences in order to
181 accommodate ADP-ribose binding. The loop between β3 and α2 (H45-V49) undergoes a change
182 in conformation and the sidechain of F132 is moved out of the ADP-ribose binding site (Fig.
183 S3C). Our ADP-ribose bound structure is nearly identical to 6W02, except for slight deviations
184 in the β3-α2 loop and an altered conformation of F156, where the aryl ring of F156 is moved
185 closer to the adenine ring (Fig. S3 C-D). However, this is likely a result of crystal packing as
186 F156 adopts this conformation in each subunit and would likely clash with subunit residues
187 related by either crystallographic or non-crystallographic symmetry.

188 We next compared the ADP-ribose bound SARS-CoV-2 Mac1 structure with that of
189 SARS-CoV (PDB 2FAV) (6) and MERS-CoV (PDB 5HOL) (31) Mac1 proteins. Superposition
190 yielded RMSD deviations of 0.71 Å (166 residues) and 1.06 Å (161 residues) for 2FAV and

191 5HOL, respectively. Additionally, the ADP-ribose binding mode in the SARS-CoV and SARS-
192 CoV-2 structures almost perfectly superimposed (Fig. 4A-D). The conserved aspartic acid
193 residue (D22, SARS-CoV-2) that binds to adenine, are localized in a similar region although
194 there are slight differences in the rotamers about the Cβ-Cγ bond. The angles between the mean
195 planes defined by the OD1, CG and OD2 atoms relative to SARS-CoV-2 Mac1 is 23.1° and
196 46.5° for the SARS-CoV and MERS-CoV Mac1 structures, respectively. Another notable
197 difference is that SARS-CoV and SARS-CoV-2 macrodomains have an isoleucine (I23)
198 following this aspartic acid while MERS-CoV has an alanine (A22). Conversely, SARS-CoV-2
199 and SARS-CoV Mac1 have a valine instead of an isoleucine immediately following the GGG
200 motif (V49/I48). From these structures it appears that having two isoleucines in this location
201 would clash, and that lineage B and lineage C β-CoVs has evolved in unique ways to create
202 space in this pocket (Fig. 4D and data not shown). Despite these small differences in local
203 structure, the overall structure of CoV Mac1 domains remain remarkably conserved, and
204 indicates they likely have similar biochemical activities and biological functions.

205 **SARS-CoV, SARS-CoV-2, and MERS-CoV bind to ADP-ribose with similar**
206 **affinities.** To determine if the CoV macrodomains had any noticeable differences in their ability
207 to bind ADP-ribose, we performed isothermal titration calorimetry (ITC), which measures the
208 energy released or absorbed during a binding reaction. Macrodomain proteins from human
209 (Mdo2), SARS-CoV, MERS-CoV, and SARS-CoV-2 were purified (Fig. S1A) and tested for
210 their affinity to ADP-ribose. All CoV Mac1 proteins bound to ADP-ribose with low micromolar
211 affinity (7-16 μM), while human Mdo2 bound with an affinity about 10-times stronger (~220
212 nM) (Fig. 5A-B). As a control we tested the ability of the MERS-CoV macrodomain to bind to
213 ATP, and only observed minimal binding with mM affinity (data not shown). At higher

214 concentrations, the SARS-CoV-2 macrodomain caused a slightly endothermic reaction,
215 potentially the result of protein aggregation or a change in conformation (Fig. 5A). The MERS-
216 CoV Mac1 had a greater affinity for ADP-ribose than SARS-CoV or SARS-CoV-2 Mac1 in the
217 ITC assay (Fig. 5A-B), however, our results found the differences between these macrodomain
218 proteins to be much closer than previously reported (9). As an alternate method to confirm ADP-
219 ribose binding, we conducted a thermal shift assay. All 4 macrodomains tested denatured at
220 higher temperatures with the addition of ADP-ribose (Fig. S4). We then tested the ability of the
221 CoV Mac1 proteins to bind to PAR using a PAR overlay assay. Macrodomain proteins were slot-
222 blotted onto a nitrocellulose membrane and were then incubated with purified PAR. PAR
223 binding was then detected with 2 distinct anti-PAR antibodies (Fig. 5C). Histone H1, which
224 binds very efficiently to PAR, and DNaseI were used as positive and negative controls,
225 respectively, as described previously (32). This assay showed that Mdo2 and MERS-CoV Mac1
226 could bind to PAR, in contrast to SARS-CoV or SARS-CoV-2 Mac1, which were unable to bind
227 PAR. Importantly, only 1 pmol of Histone H1 was needed to bind to PAR, while 60 pmol of the
228 macrodomain proteins were used to detect PAR binding. We conclude that lineage B and lineage
229 C β-CoV Mac1 proteins bind to ADP-ribose with similar affinities, but demonstrate unique
230 differences in their ability to bind PAR.

231 **CoV macrodomains are highly efficient MAR-hydrolases.** To examine the MAR-
232 hydrolase activity of CoV Mac1, we first tested the viability of using antibodies to detect
233 MARylated protein. Previously, radiolabeled $NAD^+$ has been the primary method used to label
234 MARylated protein (14, 15). To create a MARylated substrate, the catalytic domain of the
235 PARP10 (GST-PARP10 CD) protein was incubated with $NAD^+$, leading to its automodification.
236 We then tested a panel of monoclonal antibodies that detect MAR, PAR, or both MAR and PAR

237 for the ability to detect MARylated PARP10. The anti-MAR and anti-MAR/PAR antibodies, but
238 not anti-PAR antibody, bound to MARylated PARP10 (Fig. S5). From herein we utilized the
239 anti-MAR antibody to detect MARylated PARP10.

240 We next tested the ability of SARS-CoV-2 Mac1 to remove ADP-ribose from
241 MARylated PARP10. SARS-CoV-2 Mac1 and MARylated PARP10 were incubated at
242 equimolar amounts of protein at 37$^{o}$C and the reaction was stopped at 5, 10, 20, 30, 45 or 60
243 minutes (Fig. 6A). As a control, MARylated PARP10 was incubated alone for 60 minutes at
244 37$^{o}$C. Each reaction had equivalent amounts of MARylated PARP10 and Mac1 which was
245 confirmed by Coomassie Blue staining (Fig. 6A). An immediate reduction of more than 50%
246 band intensity was observed within five minutes, and the ADP-ribose modification was nearly
247 completely removed by SARS-CoV-2 Mac1 within 30 minutes (Fig. 6A). The MARylated
248 PAPR10 bands intensities were calculated, plotted, and fit to a non-linear regression curve (Fig.
249 6B). This result indicates that the SARS-CoV-2 Mac1 protein is a highly efficient MAR-
250 hydrolase.

251 Next, we compared MAR-hydrolase activity of Mac1 from SARS-CoV-2, SARS-CoV,
252 and MERS-CoV and human Mdo2. These proteins were incubated with MARylated PARP10 as
253 described above and the removal of MAR was analyzed at 5, 15 and 30 minutes (Fig. 6C). MAR
254 was rapidly removed from MARylated PARP10 with the CoV Mac1 proteins (Fig. 6D).
255 Approximately 95% of MAR was removed by SARS-CoV and SARS-CoV-2 Mac1 within 15
256 minutes, while at the same timepoint MERS-CoV Mac1 removed about 85% of MAR (Fig. 6D).
257 A more gradual decrease of MARylated PAPR10 band intensity was observed with Mdo2. It
258 removed approximately 70% of MAR in 30 minutes, which was significantly different from both
259 SARS-CoV and SARS-CoV-2 Mac1. These data showed that CoV Mac1 proteins have similar

260 MAR-hydrolase activity against an auto-modified PARP10 protein, and they have increased
261 activity when compared to the human Mdo2 protein under these conditions. However, further
262 enzymatic analyses of these proteins are warranted to more thoroughly understand their kinetics
263 and affinities for various MARylated substrates.

264 **CoV Mac1 proteins do not hydrolyze PAR.** To determine if the CoV Mac1 proteins
265 could remove PAR from proteins, we incubated these proteins with an auto-PARylated PARP1
266 protein. PARP1 was incubated with increasing concentrations of $NAD^+$ to create a range of
267 modification levels (Fig. S6). We incubated both partially and heavily modified PARP1 with all
268 four macrodomains and PARG as a positive control for 1 hour. While PARG completely
269 removed PAR, none of the macrodomain proteins removed PAR chains from PARP1 (Fig. 6E).
270 We conclude that macrodomain proteins are unable to remove PAR from an automodified
271 PARP1 protein under these conditions.

272 **ELISA assays can be used to measure ADP-ribosylhydrolase activity of**
273 **macrodomains.** Gel based assays as described above suffer from significant limitations in the
274 number of samples that can be done at once. A higher throughput assay will be needed to more
275 thoroughly investigate the activity of these enzymes and to screen for inhibitor compounds.
276 Based on the success of our antibody-based detection of MAR, we developed an ELISA assay
277 that has a similar ability to detect de-MARylation as our gel-based assay, but with the ability to
278 do so in a higher throughput manner (Fig. 7A). First, MARylated PARP10 was added to ELISA
279 plates. Next, the wells were washed and then incubated with different concentrations of the
280 SARS-CoV-2 Mac1 protein for 30 min. After incubation, the wells were washed and treated with
281 anti-MAR antibody, followed by HRP-conjugated secondary antibody and the detection reagent.
282 As controls, we detected MARylated and non-MARylated PARP10 proteins bound to

283 glutathione plates with anti-GST and anti-MAR antibodies as primary and their corresponding
284 secondary antibodies (Fig. 7B). SARS-CoV-2 Mac1 was able to remove MAR signal in a dose-
285 dependent manner and fit to a non-linear regression curve (Fig. 7C). Based on these results, we
286 conclude that this ELISA assay will be a useful tool for screening potential inhibitors or defining
287 enzyme kinetics of macrodomain proteins.

288 **DISCUSSION**

289 Here we report the crystal structure of SARS-CoV-2 Mac1 and its enzyme activity *in*
290 *vitro*. Structurally, it has a conserved three-layered α/β/α fold typical of the MacroD family of
291 macrodomains, and is extremely similar to other CoV Mac1 proteins (Fig. 2-4). The conserved
292 CoV macrodomain (Mac1) was initially described as an ADP-ribose-1”-phosphatase (ADRP), as
293 it was shown to be structurally similar to yeast enzymes that have this enzymatic activity (33).
294 Early biochemical studies confirmed this activity for CoV Mac1, though its phosphatase activity
295 for ADP-ribose-1”-phosphate was rather modest (6-8). Later, it was shown that mammalian
296 macrodomain proteins could remove ADP-ribose from protein substrates, indicating protein de-
297 ADP-ribosylation as a more likely function for the viral macrodomains (30, 34, 35). Shortly
298 thereafter, the SARS-CoV, hCoV-229E, FIPV, several alphavirus, and the hepatitis E virus
299 macrodomains were demonstrated to have de-ADP-ribosylating activity (14-16). However, this
300 activity has not yet been reported for the MERS-CoV or SARS-CoV-2 Mac1 protein.

301 In this study, we show that the Mac1 proteins from SARS-CoV, MERS-CoV and SARS-
302 CoV-2 hydrolyze MAR from a protein substrate (Fig. 6). Their activities were similar despite
303 sequence divergence of almost 60% between SARS-CoV-2 and MERS-CoV. We then compared
304 these activities to the human Mdo2 macrodomain. Mdo2 had a greater affinity for ADP-ribose
305 than the viral enzymes, but had significantly reduced enzyme activity in our experiments.
306 However, it’s possible that the Mdo2 and potentially the MERS-CoV Mac1 proteins were
307 partially inhibited by the released MAR in these assays due to their tighter binding to ADP-
308 ribose. Regardless, these results suggest that the human and viral enzymes likely have structural
309 differences that result in alterations in their biochemical activities *in vitro*.

310 We also compared the ability of these macrodomain proteins to bind and hydrolyze PAR.
311 None of the macrodomains were able to hydrolyze either partially or heavily modified PARP1,
312 further demonstrating that the primary enzyme activity of these proteins is to hydrolyze MAR
313 (Fig. 6E). Intriguingly, the Mdo2 and MERS-CoV macrodomain proteins bound to poly-ADP-
314 ribose, while the SARS-CoV-2 and SARS-CoV proteins did not (Fig. 5C). It is unclear if this
315 binding is relevant during infection, as these proteins do not bind to PAR nearly as well as
316 prominent PAR binding proteins, such as Histone H1, APFL, CHFR, DNA ligase 3, and XRCC1
317 (Fig. 5C) (36). From a structural standpoint it is unclear why MERS-CoV would bind PAR while
318 the other CoV Mac1 proteins do not. Further investigation is needed to understand the PAR
319 binding ability of these macrodomains, such as determining the length of PAR chains they bind
320 to, and if it is relevant for their true biological functions.
321 While all previous studies of macrodomain de-ADP-ribosylation have primarily used
322 radiolabeled substrate, we obtained highly repeatable and robust data utilizing antibodies
323 designed to specifically recognize MAR and PAR (37, 38). The use of these antibodies should
324 enhance the feasibility of this assay for many labs that are not equipped for radioactive work.
325 Utilizing these antibodies, we further developed an ELISA assay for de-MARylation that has the
326 ability to dramatically increase the number of samples that can be analyzed compared to the gel-
327 based assay. To our knowledge, previously developed ELISA assays were to measure the ADP-
328 ribosyltransferase activities (39) but no ELISA has been established to test the ADP-
329 ribosylhydrolase activity of macrodomain proteins. This ELISA assay should be useful to those
330 in the field for defining enzyme kinetics and screening compounds for macrodomain inhibitors
331 that could be either valuable research tools or potential therapeutics.

332 The functional importance of Mac1 has been demonstrated in several reports, mostly
333 utilizing the mutation of a highly conserved asparagine that mediates contact with the distal
334 ribose (Fig. 3B) (16, 19, 20). However, the proteins that are targeted by the CoV Mac1 for de-
335 ADP-ribosylation remains unknown. Regardless, from these reports it is clear that CoV Mac1 is
336 vital for the ability of these viruses to cause disease, and have indicated that it could be a novel
337 therapeutic target. Despite this, there are no known compounds that inhibit this domain. The
338 outbreak of COVID-19 has illustrated an incredible need for developing multiple therapeutic
339 drugs targeting conserved coronavirus proteins. Mac1 appears to be an ideal candidate for further
340 drug development based on its: *i)* highly conserved structure and biochemical activities within
341 CoVs; and *ii)* clear importance for multiple CoVs to cause disease. Targeting Mac1 may also
342 have the benefit of enhancing the innate immune response, as we have shown that Mac1 is
343 required for some CoVs to block IFN production (16, 21). Considering that Mac1 proteins from
344 divergent αCoVs such as 229E and FIPV also have de-ADP-ribosylating activity (14, 15), it is
345 possible that compounds targeting Mac1 could prevent disease caused by of wide variety of
346 CoV, including those of veterinary importance like porcine epidemic diarrhea virus (PEDV).
347 Additionally, compounds that inhibit Mac1 in combination with the structure could help identify
348 the mechanisms it uses to bind to its biologically relevant protein substrates, remove ADP-ribose
349 from these proteins, and potentially define the precise function for Mac1 in SARS-CoV-2
350 replication and pathogenesis. In conclusion, the results described here will be critical for the
351 design and development of highly-specific Mac1 inhibitors that could be used therapeutically to
352 mitigate COVID-19 or future CoV outbreaks.
353

354 **METHODS**

355 **Plasmids**

356 The SARS-CoV macrodomain (Mac1) (residues 1000-1172 of pp1a) was cloned into the
357 pET21a+ expression vector with an N-terminal His tag. The MERS-CoV Mac1 (residues 1110-
358 1273 of pp1a) was also cloned into pET21a+ with a C-terminal His tag. SARS-CoV-2 Mac1
359 (residues 1023-1197 of pp1a) was cloned into the pET30a+ expression vector with an N-terminal
360 His tag and a TEV cleavage site (Synbio). The pETM-CN Mdo2 Mac1 (residues 7-243)
361 expression vector with an N-terminal His-TEV-V5 tag and the pGEX4T-PARP10-CD (residues
362 818-1025) expression vector with an N-terminal GST tag were previously described (30). All
363 plasmids were confirmed by restriction digest, PCR, and direct sequencing.

364 **Protein Expression and Purification**

365 A single colony of *E. coli* cells (C41(DE3)) containing plasmids harboring the constructs
366 of the macrodomain proteins was inoculated into 10 mL LB media and grown overnight at 37°C
367 with shaking at 250 rpm. The overnight culture was transferred to a shaker flask containing 2X
368 1L TB media at 37ºC until the OD600 reached 0.7. The proteins were either induced with 0.4
369 mM IPTG at 37ºC for 3 hours, or 17°C for 20 hours. Cells were pelleted at 3500 × g for 10 min
370 and frozen at -80°C. Frozen cells were thawed at room temperature, resuspended in 50 mM Tris
371 (pH 7.6), 150 mM NaCl, and sonicated using the following cycle parameters: Amplitude: 50%,
372 Pulse length: 30 seconds, Number of pulses: 12, while incubating on ice for >1min between
373 pulses. The soluble fraction was obtained by centrifuging the cell lysate at 45,450 × g for 30
374 minutes at 4°C. The expressed soluble proteins were purified by affinity chromatography using
375 a 5 ml prepacked HisTrap HP column on an AKTA Pure protein purification system (GE
376 Healthcare). The fractions were further purified by size-exclusion chromatography (SEC) with a

377 Superdex 75 10/300 GL column equilibrated with 20mM Tris (pH 8.0), 150 mM NaCl and the
378 protein sized as a monomer relative to the column calibration standards. To cleave off the His tag
379 from the SARS-CoV-2 Mac1, purified TEV protease was added to purified SARS-CoV-2 Mac1
380 protein at a ratio of 1:10 (w/w), and then passed back through the Ni-NTA HP column. Protein
381 was collected in the flow through and equilibrated with 20 mM Tris (pH 8.0), 150 mM NaCl.
382 The SARS-CoV-2 Mac1, free from the N-terminal 6X-His tag, was used for subsequent
383 crystallization experiments.

384 For the PARP10-CD protein, the cell pellet was resuspended in 50 mM Tris-HCl (pH
385 8.0), 500 mM NaCl, 0.1mM EDTA, 25% glycerol, 1 mM DTT and sonicated as described above.
386 The cell lysate was incubated with 10 ml of Glutathione Sepharose 4B resin from GE Healthcare,
387 equilibrated with the same buffer for 2 hours, then applied to a gravity flow column to allow
388 unbound proteins to flow through. The column was washed with the resuspension buffer till the
389 absorbance at 280 nm reached baseline. The bound protein was eluted out of the column with
390 resuspension buffer containing 20 mM reduced glutathione and then dialyzed back into the
391 resuspension buffer overnight at 4°C.

392 **Isothermal Titration Calorimetry**

393 All ITC titrations were performed on a MicroCal PEAQ-ITC instrument (Malvern
394 Pananalytical Inc., MA). All reactions were performed in 20 mM Tris pH 7.5, 150 mM NaCl
395 using 100 μM of all macrodomain proteins at 25°C. Titration of 2 mM ADP-ribose or ATP
396 (MilliporeSigma) contained in the stirring syringe included a single 0.4 μL injection, followed by
397 18 consecutive injections of 2 μL. Data analysis of thermograms was analyzed using one set of
398 binding sites model of the MicroCal ITC software to obtain all fitting model parameters for the
399 experiments.

400 **Differential Scanning Fluorimetry (DSF)**

401 Thermal shift assay with DSF involved use of LightCycler® 480 Instrument (Roche
402 Diagnostics). In total, a 15 µL mixture containing 8X SYPRO Orange (Invitrogen), and 10 µM
403 macrodomain protein in buffer containing 20 mM Hepes, NaOH, pH 7.5 and various
404 concentrations of ADP-ribose were mixed on ice in 384-well PCR plate (Roche). Fluorescent
405 signals were measured from 25 to 95 °C in 0.2 °C/30-s steps (excitation, 470-505 nm; detection,
406 540-700 nm). The main measurements were carried out in triplicate. Data evaluation and Tm
407 determination involved use of the Roche LightCycler® 480 Protein Melting Analysis software,
408 and data fitting calculations involved the use of single site binding curve analysis on Graphpad
409 Prism.

410 **De-MARylation Assays**

411 *Automodification of PARP10-CD protein*: A 10 µM solution of purified PAPR10-CD
412 protein was incubated for 20 minutes at 37ºC with 1 mM final concentration of β-Nicotinamide
413 Adenine Dinucleotide (β $NAD^+$) (Millipore-Sigma) in a reaction buffer (50 mM HEPES, 150
414 mM NaCl, 0.2 mM DTT, and 0.02% NP-40). MARylated PARP10 was aliquoted and stored at -
415 80ºC.

416 *PAPR10-CD ADP-ribose hydrolysis:* All reactions were performed at 37ºC for the
417 designated time. A 1 µM solution of MARylated PARP10-CD and purified Mac1 protein was
418 added in the reaction buffer (50 mM HEPES, 150 mM NaCl, 0.2 mM DTT, and 0.02% NP-40).
419 The reaction was stopped with addition of 2X Laemmli sample buffer containing 10% β-
420 mercaptoethanol.

421 Protein samples were heated at 95ºC for 5 minutes before loading and separated onto
422 SDS-PAGE cassette (Thermo Fisher Scientific Bolt™ 4-12% Bis-Tris Plus Gels) in MES

423 running buffer. For direct protein detection, the SDS-PAGE gel was stained using InstantBlue®
424 Protein Stain (Expedeon). For immunoblotting, the separated proteins were transferred onto
425 polyvinylidene difluoride (PVDF) membrane using iBlot™ 2 Dry Blotting System
426 (ThermoFisher Scientific). The blot was blocked with 5% skim milk in PBS containing 0.05%
427 Tween-20 and probed with anti-mono or poly ADP-ribose binding antibodies MABE1076 (α-
428 MAR), MABC547 (α-PAR), MABE1075 (α-MAR/PAR) (Millipore-Sigma) and anti-GST tag
429 monoclonal antibody MA4-004 (ThermoFisher Scientific). The primary antibodies were detected
430 with secondary infrared anti-rabbit and anti-mouse antibodies (LI-COR Biosciences). All
431 immunoblots were visualized using Odyssey® CLx Imaging System (LI-COR Biosciences). The
432 images were quantitated using Image J software (National Institutes for Health (NIH)).
433 *ELISA-based MAR hydrolysis:* ELISA Well-Coated™ Glutathione plates (G-Biosciences,
434 USA) were washed with phosphate-buffered saline (PBS) containing 0.05% Tween-20 (PBS-T)
435 and incubated with 50 µL of 100 nM automodified MARylated PARP10-CD in PBS for one
436 hour under room temperature. Following four washes with PBS-T, variable concentrations of
437 SARS-CoV-2 Mac1 were incubated with MARylated PARP10-CD for 30 minutes at 37$^{o}$C.
438 Purified macrodomains were 2-fold serially diluted starting at 100 nM in reaction buffer prior to
439 addition to MARylated PARP10-CD. Subsequently, ELISA wells were washed four times with
440 PBS-T and incubated with 50 µL/well of anti-GST (Invitrogen MA4-004) or anti-MAR
441 (Millipore-Sigma MAB1076) diluted 1:5,000 in 5 mg/ml BSA in PBS-T (BSA5-PBS-T) for 1
442 hour at room temperature. After four additional washes with PBS-T, each well was incubated
443 with 50 µL diluted 1:5,000 in BSA5-PBS-T of anti-rabbit-HRP (SouthernBiotech, USA) or anti-
444 mouse-HRP (Rockland Immunochemicals, USA) conjugate for 1 hour at room temperature. The
445 plate was washed four times with PBS-T and 100 µL of TMB peroxidase substrate solution

446 (SouthernBiotech, USA) was added to each well and incubated for 10 minutes. The peroxidase
447 reaction was stopped with 50 µL per well of 1 M HCl before proceeding to reading. Absorbance
448 was measured at 450 nm and subtracted from 620 nm using Biotek Powerwave XS plate reader
449 (BioTek). As controls, MARylated PARP10-CD and non-MARylated PARP10 were detected
450 with both anti-MAR and anti-GST antibodies. The absorbance of non-MARylated PARP10-CD
451 detected with anti-MAR antibody was used to establish the background signal. The % signal
452 remaining was calculated by dividing the experimental signal (+ enzyme) minus background by
453 the control (no enzyme) minus the background.

454 **PAR Binding Assay**

455 Proteins were slot-blotted on a 0.2 µm pore–size nitrocellulose membrane (Bio-Rad)
456 using a Bio-Dot® microfiltration apparatus (Bio-Rad). Sixty picomoles of macrodomain proteins
457 Mdo2, SARS-CoV, MERS-CoV and SARS-CoV-2 diluted in 200 µL TBS (20 mM Tris-HCl pH
458 7.5, 150 mM NaCl) were applied to the vacuum manifold sample template. Calf thymus histone
459 H1 (Calbiochem) and DNAse I (Roche) were respectively used as positive and negative PAR-
460 binding proteins. Following complete aspiration of the protein samples, the nitrocellulose
461 membrane was rinsed three times in 50 mL TBS-T (20 mM Tris-HCl pH 7.5, 150 mM NaCl,
462 0.01% Tween-20). The membrane was incubated with TBS-T containing 100 nM PAR purified
463 by dihydroxyboronyl Bio-Rex (DHBB) chromatography (40). The membranes were extensively
464 washed with TBS-T and blocked with a PBS-MT solution (PBS supplemented with 5% milk and
465 0.1% Tween-20) for 1 hour. The membrane was then incubated with the anti-PAR monoclonal
466 antibody clone 10H (Tulip Biolabs) or the polyclonal antibody 96-10 (38) for 1 hour. The
467 membrane was extensively washed with PBS-T and incubated with the corresponding
468 peroxidase-conjugated secondary antibodies (Jackson ImmunoResearch) for 30 min. The

469 membrane was finally washed three times with PBS-T and signal was detected using the Western
470 Lightning® Plus ECL chemiluminescence substrate (PerkinElmer). SYPRO™ Ruby protein blot
471 stain was used according to the manufacturer's protocol (Bio-Rad) to assess the efficiency of
472 protein transfer to the nitrocellulose membrane. Fluorescence imaging was acquired using a
473 Geliance CCD-based bioimaging system (PerkinElmer).

474 **De-PARylation Assay**

475 *Automodification of PARP1 protein*: PARP1 was incubated with increasing
476 concentrations of $NAD^+$ to generate a range of PARP1 automodification levels. Highly purified
477 human 6X-His-PARP1 (41) (5 µg) was incubated for 30 min at 30°C in a reaction buffer
478 containing 100 mM Tris-HCl pH 8.0, 10 mM $MgCl_2$, 10% (v/v) glycerol, 10 mM DTT, 0 to 500
479 µM NAD+, 10% (v/v) ethanol and 25 µg/mL calf thymus activated DNA (Sigma-Aldrich).

480 *PARP1 ADP-ribose hydrolysis:* To evaluate the PAR hydrolase activity of CoV
481 macrodomains, 200 ng of slightly automodified PARP1 with 5 µM $NAD^+$ or highly
482 automodified with 500 µM $NAD^+$ were used as substrates for the de-PARylation assays.
483 Recombinant macrodomain protein (1 µg) was supplemented to the reaction buffer (100 mM
484 Tris-HCl pH 8.0, 10% (v/v) glycerol and 10 mM DTT) containing automodified PARP1 and
485 incubated for 1 hour at 37$^o$C. Recombinant PARG (1 µg) was used as a positive control for PAR
486 erasing (42). Reaction mixtures were resolved on 4–12% Criterion™ XT Bis-Tris protein gels,
487 transferred onto nitrocellulose membrane and probed with the anti-PAR polyclonal antibody 96-
488 10 as described for the polymer-blot assays.

489 **Structure Determination**

490 *Crystallization and Data Collection*: Purified SARS-CoV-2 Mac1 in 150 mM NaCl, 20
491 mM Tris pH 8.0 was concentrated to 13.8 mg/mL for crystallization screening. All crystallization

492 experiments were setup using an NT8 drop-setting robot (Formulatrix Inc.) and UVXPO MRC
493 (Molecular Dimensions) sitting drop vapor diffusion plates at 18°C. 100 nL of protein and 100
494 nL crystallization solution were dispensed and equilibrated against 50 µL of the latter. The
495 SARS-CoV-2 Mac1 complex with ADP-ribose was prepared by adding the ligand, from a 100
496 mM stock in water, to the protein at a final concentration of 2 mM. Crystals that were obtained in
497 1-2 days from the Salt Rx HT screen (Hampton Research) condition E10 (1.8 M
498 $NaH_2PO_4/K_2HPO_4$, pH 8.2). Refinement screening was conducted using the additive screen HT
499 (Hampton Research) by supplementing 10% of each additive to the Salt Rx HT E10 condition in
500 a new 96-well UVXPO crystallization plate. The crystals used for data collection were obtained
501 from Salt Rx HT E10 supplemented with 0.1 M NDSB-256 from the additive screen (Fig. S1).
502 Samples were transferred to a fresh drop composed of 80% crystallization solution and 20%
503 (v/v) PEG 200 and stored in liquid nitrogen. X-ray diffraction data were collected at the
504 Advanced Photon Source, IMCA-CAT beamline 17-ID using a Dectris Eiger 2X 9M pixel array
505 detector.

506 *Structure Solution and Refinement*: Intensities were integrated using XDS (43, 44) via
507 Autoproc (45) and the Laue class analysis and data scaling were performed with Aimless (46).
508 Notably, a pseudo-translational symmetry peak was observed at (0, 0.31 0.5) that was 44.6% of
509 the origin. Structure solution was conducted by molecular replacement with Phaser (47) using a
510 previously determined structure of ADP-ribose bound SARS-CoV-2 Mac1 (PDB 6W02) as the
511 search model. The top solution was obtained in the space group $P2_1$ with four molecules in the
512 asymmetric unit. Structure refinement and manual model building were conducted with Phenix
513 (48) and Coot (49) respectively. Disordered side chains were truncated to the point for which
514 electron density could be observed. Structure validation was conducted with Molprobity (50) and

515 figures were prepared using the CCP4MG package (51). Superposition of the macrodomain
516 structures was conducted with GESAMT (52).

517 **Statistical Analysis**

518 All statistical analyses were done using an unpaired two-tailed student's t-test to assess
519 differences in mean values between groups, and graphs are expressed as mean ±SD. Significant p
520 values are denoted with *$p \leq 0.05$.

521 **ACCESSION CODES**

522 The coordinates and structure factors for SARS-CoV-2 Mac1 were deposited to the
523 Worldwide Protein Databank (wwPDB) with the accession code 6WOJ.

524 **ACKNOWLEDGEMENTS**

525 We'd like to thank Ivan Ahel and Gytis Jankevicius (Oxford University) for providing
526 protein expression plasmids; John Pascal (University of Montreal) and Marie-France Langelier
527 (Universite de Montreal) for providing PARP1; and Wenqing Xu (University of Washington) for
528 providing PARG. This research was funded by the National Institutes of Health (NIH), grant
529 numbers P20 GM113117, P30GM110761, and AI134993-01 to A.R.F and the Canadian
530 Institutes of Health Research, grant number MOP-418863 to G.G.P. Use of the IMCA-CAT
531 beamline 17-ID at the Advanced Photon Source was supported by the companies of the
532 Industrial Macromolecular Crystallography Association through a contract with Hauptman-
533 Woodward Medical Research Institute. Use of the Advanced Photon Source was supported by
534 the U.S. Department of Energy, Office of Science, Office of Basic Energy Sciences, under
535 Contract No. DE-AC02-06CH11357.

536

537 **AUTHOR CONTRIBUTIONS**

538 Conceptualization: ARF, YMOA, GGP

539 Data curation: YMOA, SL, ARF

540 Formal analysis: YMOA, DKJ, AR, SL, ARF

541 Funding acquisition: GGP, SL, ARF

542 Investigation: YMOA, MMK, AR, JPG, LN, PM, KPB

543 Methodology: YMOA, GGP, AR, JPG, SL, ARF

544 Project administration: GGP, SL, ARF

545 Resources: PG, ARF

546 Supervision: GGP, SL ARF

547 Validation: YMOA, SL, AR, JPG, GGP, ARF

548 Visualization: YMOA, ARF, AR, SL, JPG

549 Writing – original draft: YMOA, SL, ARF

550 Writing – review & editing: all authors

551

552 **REFERENCES**
553

554 1. Zhou P, Yang XL, Wang XG, Hu B, Zhang L, Zhang W, Si HR, Zhu Y, Li B, Huang CL,
555 Chen HD, Chen J, Luo Y, Guo H, Jiang RD, Liu MQ, Chen Y, Shen XR, Wang X, Zheng
556 XS, Zhao K, Chen QJ, Deng F, Liu LL, Yan B, Zhan FX, Wang YY, Xiao GF, Shi ZL.
557 2020. A pneumonia outbreak associated with a new coronavirus of probable bat origin.
558 Nature 579:270-273.
559 2. Coronaviridae Study Group of the International Committee on Taxonomy of V. 2020.
560 The species Severe acute respiratory syndrome-related coronavirus: classifying 2019-
561 nCoV and naming it SARS-CoV-2. Nat Microbiol 5:536-544.
562 3. Srinivasan S, Cui H, Gao Z, Liu M, Lu S, Mkandawire W, Narykov O, Sun M, Korkin D.
563 2020. Structural Genomics of SARS-CoV-2 Indicates Evolutionary Conserved
564 Functional Regions of Viral Proteins. Viruses 12:360.
565 4. Wu C, Liu Y, Yang Y, Zhang P, Zhong W, Wang Y, Wang Q, Xu Y, Li M, Li X, Zheng
566 M, Chen L, Li H. 2020. Analysis of therapeutic targets for SARS-CoV-2 and discovery
567 of potential drugs by computational methods. Acta Pharm Sin B
568 doi:10.1016/j.apsb.2020.02.008.
569 5. Fehr AR, Perlman S. 2015. Coronaviruses: An Overview of Their Replication and
570 Pathogenesis, p 1-23. *In* Maier HJ, Bickerton E, Britton P (ed), Coronaviruses, vol 1282.
571 Springer New York.
572 6. Egloff MP, Malet H, Putics A, Heinonen M, Dutartre H, Frangeul A, Gruez A,
573 Campanacci V, Cambillau C, Ziebuhr J, Ahola T, Canard B. 2006. Structural and
574 functional basis for ADP-ribose and poly(ADP-ribose) binding by viral macro domains. J
575 Virol 80:8493-502.
576 7. Putics A, Filipowicz W, Hall J, Gorbalenya AE, Ziebuhr J. 2005. ADP-ribose-1"-
577 monophosphatase: a conserved coronavirus enzyme that is dispensable for viral
578 replication in tissue culture. J Virol 79:12721-31.
579 8. Saikatendu KS, Joseph JS, Subramanian V, Clayton T, Griffith M, Moy K, Velasquez J,
580 Neuman BW, Buchmeier MJ, Stevens RC, Kuhn P. 2005. Structural basis of severe acute
581 respiratory syndrome coronavirus ADP-ribose-1"-phosphate dephosphorylation by a
582 conserved domain of nsP3. Structure 13:1665-75.
583 9. Cho CC, Lin MH, Chuang CY, Hsu CH. 2016. Macro Domain from Middle East
584 Respiratory Syndrome Coronavirus (MERS-CoV) Is an Efficient ADP-ribose Binding
585 Module: CRYSTAL STRUCTURE AND BIOCHEMICAL STUDIES. J Biol Chem
586 291:4894-902.
587 10. Xu YY, Cong L, Chen C, Wei L, Zhao Q, Xu XL, Ma YL, Bartlam M, Rao ZH. 2009.
588 Crystal Structures of Two Coronavirus ADP-Ribose-1 "-Monophosphatases and Their
589 Complexes with ADP-Ribose: a Systematic Structural Analysis of the Viral ADRP
590 Domain. Journal of Virology 83:1083-1092.
591 11. Makrynitsa GI, Ntonti D, Marousis KD, Birkou M, Matsoukas MT, Asami S, Bentrop D,
592 Papageorgiou N, Canard B, Coutard B, Spyroulias GA. 2019. Conformational plasticity
593 of the VEEV macro domain is important for binding of ADP-ribose. J Struct Biol
594 206:119-127.
595 12. Malet H, Coutard B, Jamal S, Dutartre H, Papageorgiou N, Neuvonen M, Ahola T,
596 Forrester N, Gould EA, Lafitte D, Ferron F, Lescar J, Gorbalenya AE, de Lamballerie X,
597 Canard B. 2009. The crystal structures of Chikungunya and Venezuelan equine

598 encephalitis virus nsP3 macro domains define a conserved adenosine binding pocket. J
599 Virol 83:6534-45.
600 13. Rack JG, Perina D, Ahel I. 2016. Macrodomains: Structure, Function, Evolution, and
601 Catalytic Activities. Annu Rev Biochem 85:431-54.
602 14. Li C, Debing Y, Jankevicius G, Neyts J, Ahel I, Coutard B, Canard B. 2016. Viral Macro
603 Domains Reverse Protein ADP-Ribosylation. J Virol 90:8478-86.
604 15. Eckei L, Krieg S, Butepage M, Lehmann A, Gross A, Lippok B, Grimm AR, Kummerer
605 BM, Rossetti G, Luscher B, Verheugd P. 2017. The conserved macrodomains of the non-
606 structural proteins of Chikungunya virus and other pathogenic positive strand RNA
607 viruses function as mono-ADP-ribosylhydrolases. Sci Rep 7:41746.
608 16. Fehr AR, Channappanavar R, Jankevicius G, Fett C, Zhao J, Athmer J, Meyerholz DK,
609 Ahel I, Perlman S. 2016. The Conserved Coronavirus Macrodomain Promotes Virulence
610 and Suppresses the Innate Immune Response during Severe Acute Respiratory Syndrome
611 Coronavirus Infection. mBio 7:e01721-16.
612 17. Kim DS, Challa S, Jones A, Kraus WL. 2020. PARPs and ADP-ribosylation in RNA
613 biology: from RNA expression and processing to protein translation and proteostasis.
614 Genes Dev 34:302-320.
615 18. Fehr AR, Singh SA, Kerr CM, Mukai S, Higashi H, Aikawa M. 2020. The impact of
616 PARPs and ADP-ribosylation on inflammation and host-pathogen interactions. Genes
617 Dev 34:341-359.
618 19. Eriksson KK, Cervantes-Barragan L, Ludewig B, Thiel V. 2008. Mouse hepatitis virus
619 liver pathology is dependent on ADP-ribose-1"-phosphatase, a viral function conserved in
620 the alpha-like supergroup. J Virol 82:12325-34.
621 20. Fehr AR, Athmer J, Channappanavar R, Phillips JM, Meyerholz DK, Perlman S. 2015.
622 The nsp3 macrodomain promotes virulence in mice with coronavirus-induced
623 encephalitis. J Virol 89:1523-36.
624 21. Grunewald ME, Chen Y, Kuny C, Maejima T, Lease R, Ferraris D, Aikawa M, Sullivan
625 CS, Perlman S, Fehr AR. 2019. The coronavirus macrodomain is required to prevent
626 PARP-mediated inhibition of virus replication and enhancement of IFN expression. PLoS
627 Pathog 15:e1007756.
628 22. Alhammad YMO, Fehr AR. 2020. The Viral Macrodomain Counters Host Antiviral
629 ADP-Ribosylation. Viruses 12:384.
630 23. Abraham R, Hauer D, McPherson RL, Utt A, Kirby IT, Cohen MS, Merits A, Leung
631 AKL, Griffin DE. 2018. ADP-ribosyl-binding and hydrolase activities of the alphavirus
632 nsP3 macrodomain are critical for initiation of virus replication. Proc Natl Acad Sci U S
633 A 115:E10457-E10466.
634 24. Abraham R, McPherson RL, Dasovich M, Badiee M, Leung AKL, Griffin DE. 2020.
635 Both ADP-Ribosyl-Binding and Hydrolase Activities of the Alphavirus nsP3
636 Macrodomain Affect Neurovirulence in Mice. mBio 11.
637 25. McPherson RL, Abraham R, Sreekumar E, Ong SE, Cheng SJ, Baxter VK, Kistemaker
638 HA, Filippov DV, Griffin DE, Leung AK. 2017. ADP-ribosylhydrolase activity of
639 Chikungunya virus macrodomain is critical for virus replication and virulence. Proc Natl
640 Acad Sci U S A 114:1666-1671.
641 26. Parvez MK. 2015. The hepatitis E virus ORF1 'X-domain' residues form a putative
642 macrodomain protein/Appr-1"-pase catalytic-site, critical for viral RNA replication. Gene
643 566:47-53.

644 27. Vuksanovic N, Silvaggi, N.R. National Science Foundation (NSF, United States). 2020.
645 High-resolution structure of the SARS-CoV-2 NSP3 Macro X domain doi:
646 10.2210/pdb6WEY/pdb. doi:10.2210/pdb6WEY/pdb.
647 28. Michalska K, Stols, L., Jedrzejczak, R., Endres, M., Babnigg, G., Kim, Y., Joachimiak,
648 A., Center for Structural Genomics of Infectious Diseases (CSGID). 2020. Crystal
649 Structure of ADP ribose phosphatase of NSP3 from SARS-CoV-2 in the apo doi:
650 10.2210/pdb6WEN/pdb. doi:10.2210/pdb6wen/pdb.
651 29. Michalska K, Kim, Y., Jedrzejczak, R., Maltseva, N., Endres, M., Mececar, A.,
652 Joachimiak, A., Center for Structural Genomics of Infectious Diseases (CSGID). 2020.
653 Crystal Structure of ADP ribose phosphatase of NSP3 from SARS CoV-2 in the complex
654 with ADP ribose doi: 10.2210/pdb6W02/pdb. doi:10.2210/pdb6W02/pdb.
655 30. Jankevicius G, Hassler M, Golia B, Rybin V, Zacharias M, Timinszky G, Ladurner AG.
656 2013. A family of macrodomain proteins reverses cellular mono-ADP-ribosylation. Nat
657 Struct Mol Biol 20:508-14.
658 31. Lei J, Kusov Y, Hilgenfeld R. 2018. Nsp3 of coronaviruses: Structures and functions of a
659 large multi-domain protein. Antiviral Res 149:58-74.
660 32. Malanga M, Althaus FR. 2011. Noncovalent protein interaction with poly (ADP-ribose),
661 p 67-82, Poly (ADP-ribose) Polymerase. Springer.
662 33. Shull NP, Spinelli SL, Phizicky EM. 2005. A highly specific phosphatase that acts on
663 ADP-ribose 1"-phosphate, a metabolite of tRNA splicing in Saccharomyces cerevisiae.
664 Nucleic Acids Res 33:650-60.
665 34. Rosenthal F, Feijs KL, Frugier E, Bonalli M, Forst AH, Imhof R, Winkler HC, Fischer D,
666 Caflisch A, Hassa PO, Luscher B, Hottiger MO. 2013. Macrodomain-containing proteins
667 are new mono-ADP-ribosylhydrolases. Nat Struct Mol Biol 20:502-7.
668 35. Sharifi R, Morra R, Appel CD, Tallis M, Chioza B, Jankevicius G, Simpson MA, Matic I,
669 Ozkan E, Golia B, Schellenberg MJ, Weston R, Williams JG, Rossi MN, Galehdari H,
670 Krahn J, Wan A, Trembath RC, Crosby AH, Ahel D, Hay R, Ladurner AG, Timinszky G,
671 Williams RS, Ahel I. 2013. Deficiency of terminal ADP-ribose protein glycohydrolase
672 TARG1/C6orf130 in neurodegenerative disease. EMBO J 32:1225-37.
673 36. Ahel I, Ahel D, Matsusaka T, Clark AJ, Pines J, Boulton SJ, West SC. 2008. Poly(ADP-
674 ribose)-binding zinc finger motifs in DNA repair/checkpoint proteins. Nature 451:81-5.
675 37. Gibson BA, Conrad LB, Huang D, Kraus WL. 2017. Generation and Characterization of
676 Recombinant Antibody-like ADP-Ribose Binding Proteins. Biochemistry (Mosc)
677 56:6305-6316.
678 38. Affar EB, Duriez PJ, Shah RG, Winstall E, Germain M, Boucher C, Bourassa S, Kirkland
679 JB, Poirier GG. 1999. Immunological determination and size characterization of
680 poly(ADP-ribose) synthesized in vitro and in vivo. Biochim Biophys Acta 1428:137-46.
681 39. Asokanathan C, Tierney S, Ball CR, Buckle G, Day A, Tanley S, Bristow A, Markey K,
682 Xing D, Yuen CT. 2018. An ELISA method to estimate the mono ADP-
683 ribosyltransferase activities: e.g in pertussis toxin and vaccines. Anal Biochem 540-
684 541:15-19.
685 40. Shah GM, Poirier D, Duchaine C, Brochu G, Desnoyers S, Lagueux J, Verreault A,
686 Hoflack JC, Kirkland JB, Poirier GG. 1995. Methods for biochemical study of
687 poly(ADP-ribose) metabolism in vitro and in vivo. Anal Biochem 227:1-13.

41. Langelier MF, Planck JL, Servent KM, Pascal JM. 2011. Purification of human PARP-1 and PARP-1 domains from Escherichia coli for structural and biochemical analysis. Methods Mol Biol 780:209-26.
42. Wang Z, Gagne JP, Poirier GG, Xu W. 2014. Crystallographic and biochemical analysis of the mouse poly(ADP-ribose) glycohydrolase. PLoS One 9:e86010.
43. Kabsch W. 1988. Evaluation of Single-Crystal X-Ray-Diffraction Data from a Position-Sensitive Detector. Journal of Applied Crystallography 21:916-924.
44. Kabsch W. 2010. Xds. Acta Crystallogr D Biol Crystallogr 66:125-32.
45. Vonrhein C, Flensburg C, Keller P, Sharff A, Smart O, Paciorek W, Womack T, Bricogne G. 2011. Data processing and analysis with the autoPROC toolbox. Acta Crystallogr D Biol Crystallogr 67:293-302.
46. Evans PR. 2011. An introduction to data reduction: space-group determination, scaling and intensity statistics. Acta Crystallogr D Biol Crystallogr 67:282-92.
47. McCoy AJ, Grosse-Kunstleve RW, Adams PD, Winn MD, Storoni LC, Read RJ. 2007. Phaser crystallographic software. J Appl Crystallogr 40:658-674.
48. Adams PD, Afonine PV, Bunkoczi G, Chen VB, Davis IW, Echols N, Headd JJ, Hung LW, Kapral GJ, Grosse-Kunstleve RW, McCoy AJ, Moriarty NW, Oeffner R, Read RJ, Richardson DC, Richardson JS, Terwilliger TC, Zwart PH. 2010. PHENIX: a comprehensive Python-based system for macromolecular structure solution. Acta Crystallogr D Biol Crystallogr 66:213-21.
49. Emsley P, Lohkamp B, Scott WG, Cowtan K. 2010. Features and development of Coot. Acta Crystallogr D Biol Crystallogr 66:486-501.
50. Chen VB, Arendall WB, 3rd, Headd JJ, Keedy DA, Immormino RM, Kapral GJ, Murray LW, Richardson JS, Richardson DC. 2010. MolProbity: all-atom structure validation for macromolecular crystallography. Acta Crystallogr D Biol Crystallogr 66:12-21.
51. Potterton L, McNicholas S, Krissinel E, Gruber J, Cowtan K, Emsley P, Murshudov GN, Cohen S, Perrakis A, Noble M. 2004. Developments in the CCP4 molecular-graphics project. Acta Crystallogr D Biol Crystallogr 60:2288-94.
52. Krissinel E. 2012. Enhanced fold recognition using efficient short fragment clustering. Journal of molecular biochemistry 1:76.
53. Evans P. 2006. Scaling and assessment of data quality. Acta Crystallogr D Biol Crystallogr 62:72-82.
54. Diederichs K, Karplus PA. 1997. Improved R-factors for diffraction data analysis in macromolecular crystallography. Nat Struct Biol 4:269-75.
55. Weiss MS. 2001. Global indicators of X-ray data quality. Journal of Applied Crystallography 34:130-135.
56. Evans P. 2012. Biochemistry. Resolving some old problems in protein crystallography. Science 336:986-7.
57. Karplus PA, Diederichs K. 2012. Linking crystallographic model and data quality. Science 336:1030-3.

**Table 1**. Crystallographic data for SARS-CoV-2 Mac1.

| | SARS-CoV-2 Mac1 |
|---|---|
| **Data Collection** | |
| Unit-cell parameters (Å, º) | $a$=59.72, $b$=83.17, $c$=84.24, $\beta$=94.4 |
| Space group | $P2_1$ |
| Resolution (Å)[1] | 48.41-2.20 (2.27-2.20) |
| Wavelength (Å) | 1.0000 |
| Temperature (K) | 100 |
| Observed reflections | 144,767 |
| Unique reflections | 41,586 |
| $<I/\sigma(I)>$[1] | 7.3 (1.9) |
| Completeness (%)[1] | 99.4 (99.7) |
| Multiplicity[1] | 3.5 (3.4) |
| $R_{merge}$ (%)[1,2] | 13.0 (67.0) |
| $R_{meas}$ (%)[1,4] | 15.4 (79.2) |
| $R_{pim}$ (%)[1,4] | 8.2 (41.8) |
| $CC_{1/2}$ [1,5] | 0.994 (0.849) |
| **Refinement** | |
| Resolution (Å)[1] | 42.00-2.20 |
| Reflections (working/test)[1] | 39,474/1,966 |
| $R_{factor}$ / $R_{free}$ (%)[1,3] | 19.9/25.2 |
| No. of atoms (Protein/Ligand/Water) | 4,930/144/358 |
| **Model Quality** | |
| R.m.s deviations | |
| Bond lengths (Å) | 0.011 |
| Bond angles (º) | 1.144 |
| Mean $B$-factor (Å)$^2$ | |
| All Atoms | 28.1 |
| Protein | 27.9 |
| Ligand | 26.0 |
| Water | 30.9 |
| Coordinate error (maximum likelihood) (Å) | 0.31 |
| Ramachandran Plot | |
| Most favored (%) | 97.3 |
| Additionally allowed (%) | 2.4 |

1) Values in parenthesis are for the highest resolution shell.
2) $R_{merge} = \Sigma_{hkl}\Sigma_I |I_i(hkl) - <I(hkl)>| / \Sigma_{hkl}\Sigma_I I_i(hkl)$, where $I_i(hkl)$ is the intensity measured for the $i$th reflection and $<I(hkl)>$ is the average intensity of all reflections with indices hkl.
3) $R_{factor} = \Sigma_{hkl} ||F_{obs}(hkl)| - |F_{calc}(hkl)|| / \Sigma_{hkl} |F_{obs}(hkl)|$; Rfree is calculated in an identical manner using 5% of randomly selected reflections that were not included in the refinement.
4) $R_{meas}$ = redundancy-independent (multiplicity-weighted) $R_{merge}$ (46, 53). $R_{pim}$ = precision-indicating (multiplicity-weighted) $R_{merge}$ (54, 55)
5) $CC_{1/2}$ is the correlation coefficient of the mean intensities between two random half-sets of data (56, 57)

741 **FIGURE LEGENDS**

742 **Figure 1.** The SARS-CoV-2 Mac1 is a small domain within nsp3 and is highly conserved
743 between other human CoV Mac1 protein domains. **(A)** Cartoon Schematic of the SARS-CoV-2
744 non-structural protein 3. The conserved macrodomain, or Mac1, is highlighted in yellow. **(B)**
745 Sequence alignment of Mac1 from the highly-pathogenic human CoVs. Sequences were aligned
746 using the ClustalW method from Clustal Omega online tool with manual adjustment. Identical
747 residues are bolded, shaded in grey, and marked with asterisks.

748 **Figure 2.** Structure of SARS-CoV-2 Mac1 complexed with ADP-ribose. **A)** The structure was
749 rendered as a blend through model from the N-terminus (blue) to the C-terminus (red). **B)** The
750 structure was colored by secondary structure showing sheets (magenta) and helices (green). The
751 ADP-ribose is rendered as gray cylinders with oxygens and nitrogens colored red and blue,
752 respectively.

753 **Figure 3.** Binding mode of ADP-ribose in SARS-CoV-2 Mac1. **A)** Fo-Fc Polder omit map
754 (green mesh) contoured at 3σ. **B)** Hydrogen bond interactions (dashed lines) between ADP-
755 ribose and amino acids. **C)** Interactions with water molecules. Direct hydrogen bond interactions
756 are represented by dashed lines and water mediated contacts to amino acids are drawn as solid
757 lines.

758 **Figure 4**. Structural comparison of the SARS-CoV-2 Mac1 protein with the SARS-CoV and
759 MERS-CoV Mac1 proteins. **A-B)** Superposition of SARS-CoV-2 macrodomain (magenta) with
760 coronavirus macrodomain structures. **A**) SARS-CoV Mac1 with ADP-ribose (gold) (2FAV) and
761 **B**) MERS-CoV Mac1 with ADP-ribose (teal) (5HOL). **C-D)** Superposition of SARS-CoV-2
762 Mac1 (magenta) with other coronavirus Mac1 structures highlighting the ADP-ribose binding
763 site. **C**) SARS-CoV (gold), **D**) MERS-CoV (teal). The ADP-ribose molecules are colored gray

764 for SARS-CoV-2 Mac1 (**A-D**) and are rendered as green cylinders for SARS-CoV Mac1 (panel
765 **A,C**) and MERS-CoV Mac1 (panel **B,D**).
766 **Figure 5**. Human CoVs bind to ADP-ribose with similar affinity. **A-B)** ADP-ribose binding of
767 human Mdo2 and SARS-CoV, MERS-CoV, and SARS-CoV-2 Mac1 proteins by ITC. Images in
768 **(A)** are of one experiment representative of at least 2 independent experiments. Data in **(B)**
769 represent the combined averages of multiple independent experiments for each protein. Mdo2
770 n=2; SARS-CoV n=5; MERS-CoV n=6; SARS-CoV-2 n=2. **C)** PAR overlay assay of CoV
771 macrodomains. 60 pmoles of macrodomain proteins were slot-blotted on a nitrocellulose
772 membrane and probed with 100 nM purified PAR. PAR binding was detected with 10H and 96-
773 10 anti-PAR antibodies. Histone H1 (1 pmole) and DNAse I (60 pmoles) were used as positive
774 and negative PAR binding controls, respectively. Blots were stained with Sypro Ruby as a
775 loading control. The figure is representative of at least three independent experiments.
776 **Figure 6**. SARS-CoV-2, SARS-CoV, and MERS-CoV Mac1 proteins are potent ADP-
777 ribosylhydrolases. **A,C)** The SARS-CoV-2 macrodomain **(A)** or multiple macrodomain proteins
778 **(C)** were incubated with MARylated PARP10 CD *in vitro* for the indicated times at 37°C. ADP-
779 ribosylated PARP10 CD was detected by immunoblot (IB) with anti-mono ADP-ribose antibody
780 (Millipore-Sigma MAB1076). Total PARP10 CD and macrodomain protein levels were
781 determined by Coomassie Blue (CB) staining. PARP10 CD incubated alone at 37°C was stopped
782 at 0, 30 or 60 minutes. **B,D)** level of de-MARylation was measured by quantifying band intensity
783 using Image J software. Intensity values were plotted and fit to a non-linear regression curve **(B)**
784 or as bar graphs representing the means with error bars representing standard deviation **(D)**.
785 Results in **A** and **C** are representative experiments of two and three independent experiments,
786 respectively. Data in **B** and **D** represent the combined results of two and three independent

787 experiments, respectively. Asterisks indicate statistical significance between these samples at the
788 same timepoint from samples treated with Mdo2. **E)** PAR hydrolase assays were performed with
789 PARP1 either extensively poly-ADP-ribosylated (500 μM $NAD^+$) or partially poly-ADP-
790 ribosylated (5 μM NAD+) to produce oligo-ADP-ribose. Macrodomains were incubated with
791 both automodified PARP1 substrates for 1 hour. PAR was detected by Western blot with the
792 anti-PAR antibody 96-10. PARG (catalytically active 60 kD fragment) was used as a positive
793 control. The results are representative of at least 2 independent experiments.
794 **Figure 7.** Development of an ELISA assay to detect de-MARylation. **A)** Cartoon schematic of
795 the ELISA assay. ELISA plates pre-coated with glutathione and pre-blocked were used capture
796 GST-tagged PARP10 proteins, which was used as a substrate for de-MARylation. The removal
797 of MAR was detected by anti-MAR antibodies. **B)** MARylated PARP10 (MAR+) and non-
798 MARylated PARP10 (MAR-) with no SARS-CoV-2 Mac1 as controls were detected with anti-
799 mono ADP-ribose antibody α-MAR (Millipore-Sigma MAB1076) or with anti-GST α-GST
800 (Invitrogen, MA4-004). **C)** Starting at 100 nM, 2-fold serial dilutions of the SARS-CoV-2 Mac1
801 protein was incubated in individual wells with MARylated PARP10-CD for 30 min. at 37°C**.**
802 The graph represents the combined results of 3 independent experiments.
803

804 **SUPPLEMENTAL FIGURE LEGENDS**

805 **Figure S1**. Purification and crystallization of macrodomain proteins. **A)** Macrodomain proteins
806 were purified as described in Methods. Equimolar amounts of the recombinant proteins were run
807 on a polyacrylamide gel and visualized by Coomassie staining. **B)** Crystals of SARS-CoV-2
808 Mac1 obtained with Salt Rx HT E10 supplemented with 0.1 M NDSB-256.

809 **Figure S2.** Extended residues at the C-terminus of the SARS-CoV-2 Mac1 clashed with
810 symmetry related molecules. **A)** Comparison of the amino acid sequence of SARS-CoV-2 Mac1,
811 6W02 and 6WEY. **B)** Superposition of SARS-CoV-2 Mac1 (magenta) subunit B onto subunit A
812 of 6W02 reveals that the C-terminus would clash with symmetry related molecules (coral).

813 **Figure S3**. Comparison of the SARS-CoV-2 Mac1 protein with homologous structures. **A-B)**
814 Superposition of SARS-CoV-2 Mac1 (magenta) with other recently determined homologous
815 structures. **A)** SARS-CoV-2 Mac1 apo structure (6WEN), **B)** SARS-CoV-2 Mac1 complexed
816 with ADP-ribose (6W02). The ADP-ribose molecule is colored gray for SARS-CoV-2 and is
817 represented as green cylinders for 6W02 in panel **B**. **C-D)** Comparison of the residues in the
818 ADP-ribose binding site. **C**) SARS-CoV-2 Mac1 apo structure (blue, 6WEN), **D**) SARS-CoV-2
819 Mac1 complexed with ADP-ribose (green, 6W02). The ADP-ribose of SARS-CoV-2 is rendered
820 as gray cylinders, and is represented as green cylinders for 6W02 in panel **B**.

821 **Figure S4**. ADP-ribose binding of macrodomain proteins by DSF assay. 10 μM macrodomain
822 protein was incubated with increasing concentrations of ADP-ribose and measured by DSF as
823 described in Methods. Mdo2 n=4; SARS-CoV n=6; MERS-CoV n=5; SARS-CoV-2 n=3.

824 **Figure S5**. Affinity of ADP-ribose binding antibodies for ADP-ribosylated PARP10 CD.
825 MARylated PARP10 and non-MARylated PARP10 CD were detected by immunoblot (IB) with
826 anti-GST (Invitrogen, MA4-004), anti-ADP-ribose antibodies: anti-MAR (Millipore-Sigma

827 MAB1076), anti-PAR (Millipore-Sigma MABC547), and anti-MAR/PAR (Millipore-Sigma
828 MABE1075) antibodies.
829 **Figure S6**. Differential PARylation of PARP1 by varying concentrations of $NAD^+$. Recombinant
830 human PARP1 was automodified in a reaction buffer supplemented with increasing
831 concentration of $NAD^+$ to generate substrates for the PAR hydrolase assays. The presence of
832 PAR was detected by Western blot analysis of reaction products with the anti-PAR antibody 96-
833 10.

**A**

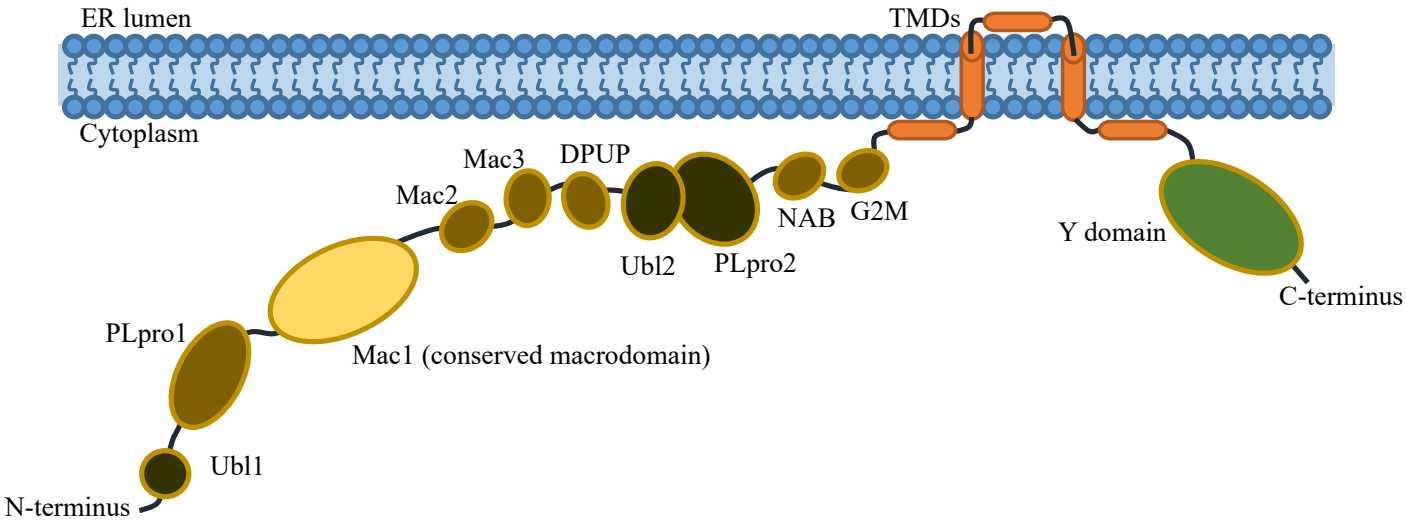


**B**

```
SARS-CoV-2 aa  1        10        20        30        40        50      58
               |         |         |         |         |         |       |
SARS-CoV-2    --IEVNSFSGYLKLTDNVYIKNADIVEEAKKVKPTVVVNAANVYLKHGGGVAGALNKATN 58
SARS-CoV      --EPVNQFTGYLKLTDNVAIKCVDIVKEAQSANPMVIVNAANIHLKHGGGVAGALNKATN 58
MERS-CoV      NVDPLSNFEHK-VITECVTIVLGDAIQVAKCYGESVLVNAANTHLKHGGGIAGAINAASK 59
                     *      *  * *   *    *      * *****  ****** *** * *
SARS-CoV-2 aa 60        70        80        90       100       110     118
               |         |         |         |         |         |       |
SARS-CoV-2    NAMQVESDDYIATNGPLKVGGSCVLSGHNLAKHCLHVVGPNVNKGEDIQLLKSAYEVFNQ 118
SARS-CoV      GAMQKESDDYIKLNGPLTVGGSCLLSGHNLAKKCLHVVGPNLNAGEDIQLLKAAYENFNS 118
MERS-CoV      GAVQKESDEYILAKGPLQVGDSVLLQGHSLAKNILHVVGPDARAKQDVSLLSKCYKAMNA 119
               * * *** **   *** ** *  * ** ***  ******      *  **   *   *

SARS-CoV-2 aa 120       130       140       150       160       170
               |         |         |         |         |         |
SARS-CoV-2    HEVLLAPLLSAGIFGADPIHSLRVCVDTVRTNVYLAVFDKNLYDKLVSSFLEMKSEK  175
SARS-CoV      QDILLAPLLSAGIFGAKPLQSLQVCVQTVRTQVYIAVNDKALYEQVVMDYLDNL-    172
MERS-CoV      YPLVVTPLVSAGIFGVKPAVSFDYLIREAKTRVLVVVNSQDVYKSLTIVDIPQLE    174
                    ** ******  *  *          * *   *     *
```

**Figure 1.** The SARS-CoV-2 Mac1 is a small domain within nsp3 and is highly conserved between other human CoV Mac1 protein domains. **(A)** Cartoon Schematic of the SARS-CoV-2 non-structural protein 3. The conserved macrodomain, or Mac1, is highlighted in yellow. **(B)** Sequence alignment of Mac1 from the highly-pathogenic human CoVs. Sequences were aligned using the ClustalW method from Clustal Omega online tool with manual adjustment. Identical residues are bolded, shaded in grey, and marked with asterisks.

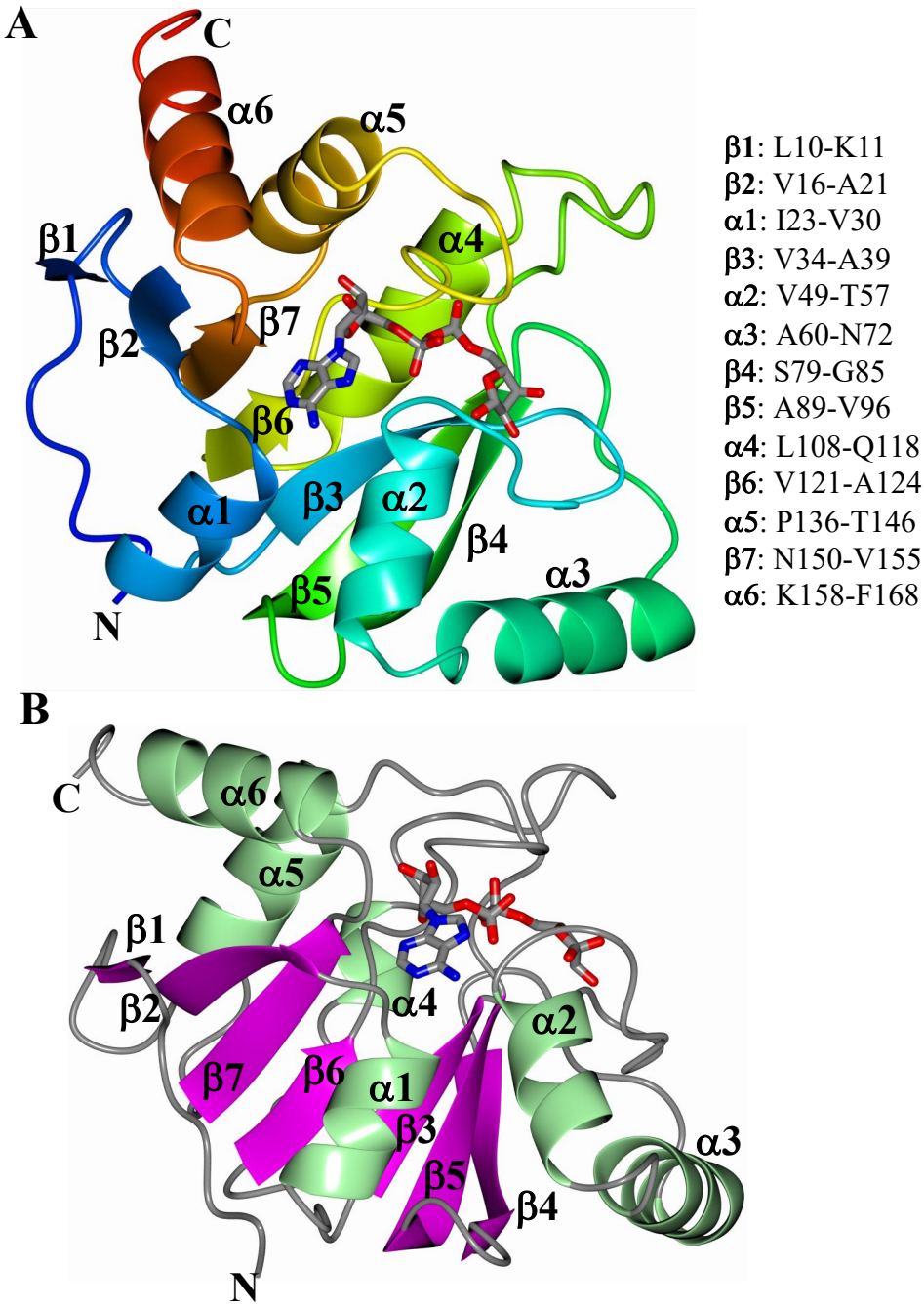


**Figure 2.** Structure of SARS-CoV-2 Mac1 complexed with ADP-ribose. **A)** The structure was rendered as a blend through model from the N-terminus (blue) to the C-terminus (red). **B)** The structure was colored by secondary structure showing sheets (magenta) and helices (green). The ADP-ribose is rendered as gray cylinders with oxygens and nitrogens colored red and blue, respectively.

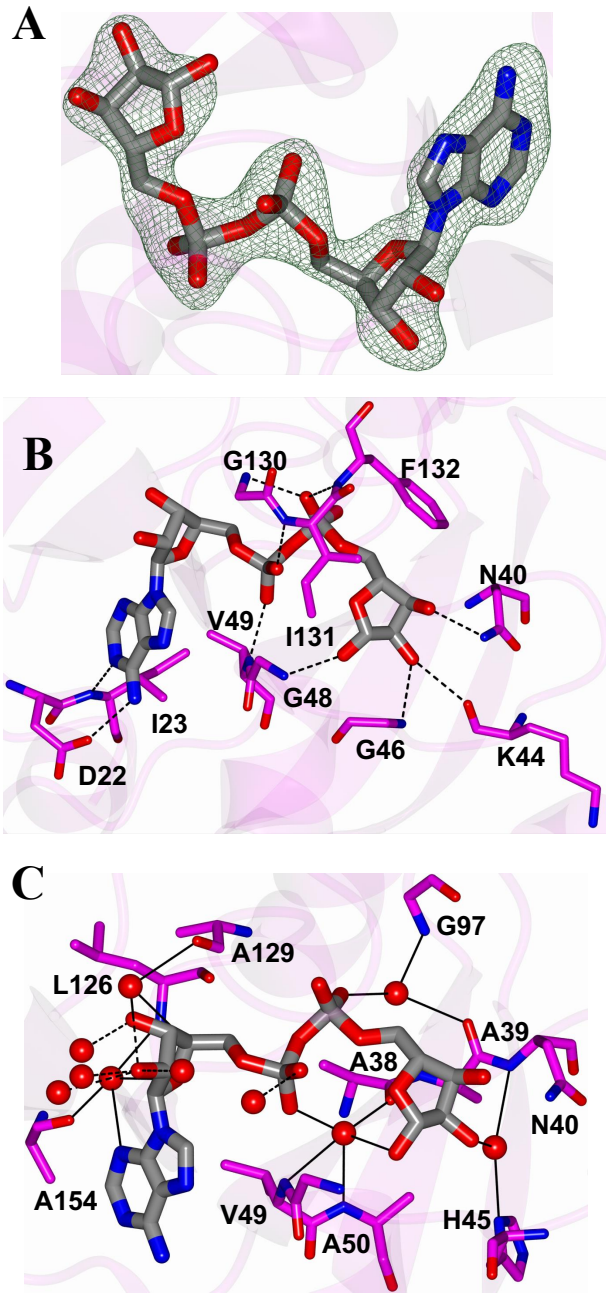


**Figure 3.** Binding mode of ADP-ribose in SARS-CoV-Mac1. **A)** Fo-Fc Polder omit map (green mesh) contoured at 3σ. **B)** Hydrogen bond interactions (dashed lines) between ADP-ribose and amino acids. **C)** Interactions with water molecules. Direct hydrogen bond interactions are represented by dashed lines and water mediated contacts to amino acids are drawn as solid lines.

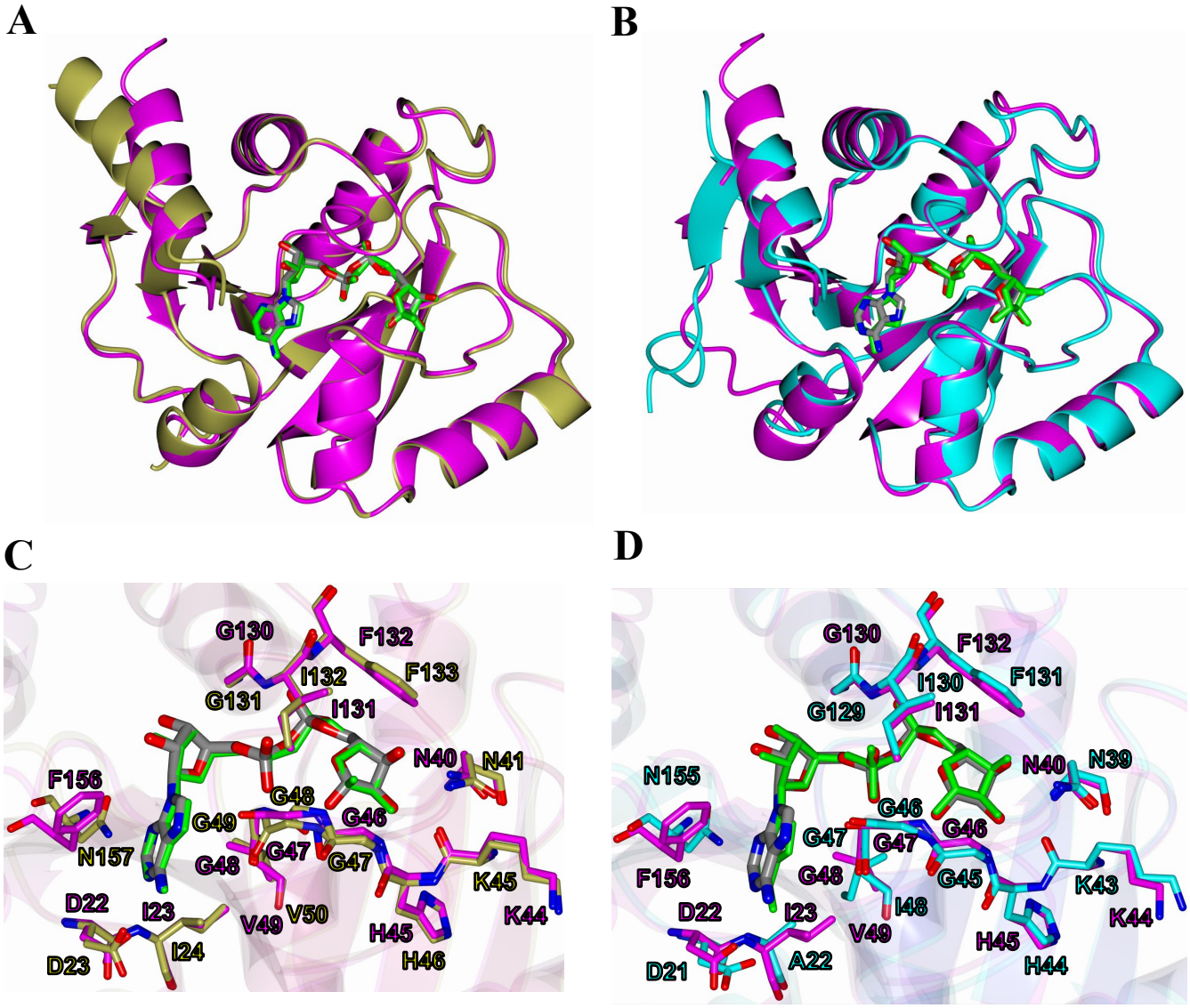


**Figure 4**. Superposition of SARS-CoV-2 macrodomain (magenta) with coronavirus macrodomain structures. **A**) SARS-CoV Mac1 with ADP-ribose (gold) (2FAV) and **B**) MERS-CoV Mac1 with ADP-ribose (teal) (5HOL). Superposition of SARS-CoV-2 Mac1 (magenta) with other coronavirus Mac1 structures highlighting the ADP-ribose binding site. **C**) SARS-CoV (gold), **D**) MERS-CoV (teal). The ADP-ribose molecules are colored gray for SARS-CoV-2 (A-D) and are rendered as green cylinders for SARS-CoV Mac1 (panel A,C) and MERS-CoV Mac1 (panel B,D).

**A**

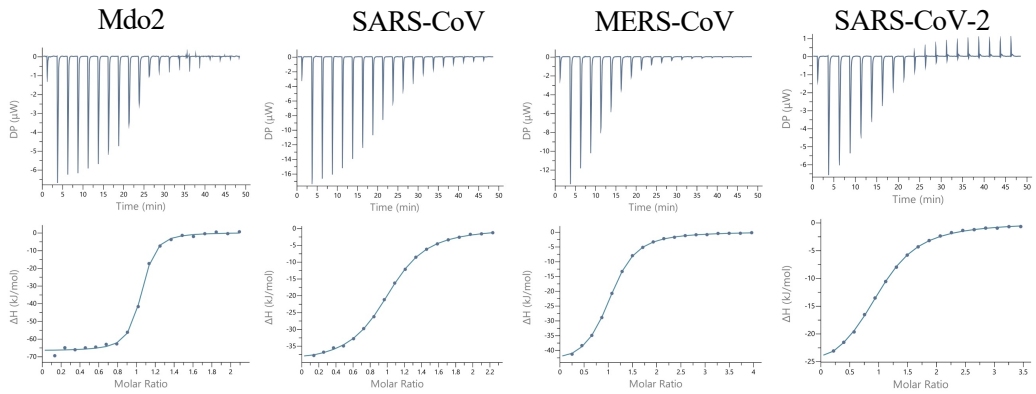


**B**

| Macrodomain | Stoichiometry (N) | Kd (uM) | ΔH (kcal/mol) | ΔG (kcal/mol) |
|---|---|---|---|---|
| Mdo2 | 0.92 ± 0.01 | 0.24 ± 0.02 | -66 ± 1 | -38 ± 2 |
| SARS-CoV | 0.89 ± 0.04 | 10.8 ± 1.7 | -40 ± 1.2 | -28 ± 0.4 |
| MERS-CoV | 0.97 ± 0.04 | 7.9 ± 0.15 | -47 ± 3 | -29 ± 0.4 |
| SARS-CoV-2 | 1.14 ± 0.06 | 16.8 ± 0.04 | -28 ± 0.1 | -27 ± 0.1 |

**C**

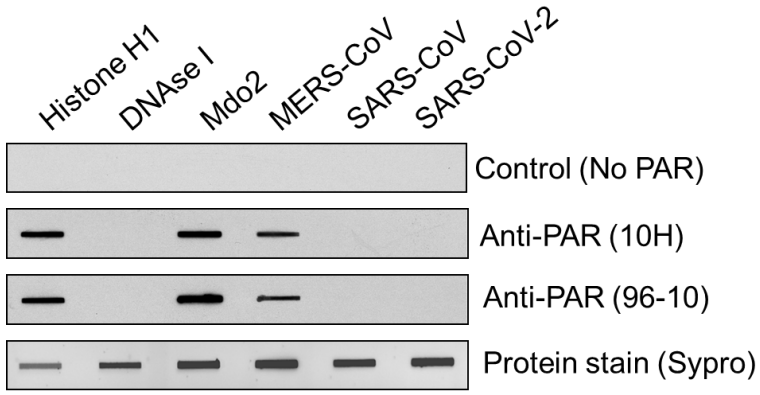


**Figure 5**. Human CoVs bind to ADP-ribose with similar affinity. **A-B)** ADP-ribose binding of human Mdo2 and SARS-CoV, MERS-CoV, and SARS-CoV-2 Mac1 proteins by ITC. Images in **(A)** are of one experiment representative of at least 2 independent experiments. Data in **(B)** represent the combined averages of multiple independent experiments for each protein. Mdo2 n=2; SARS-CoV n=5; MERS-CoV n=6; SARS-CoV-2 n=2. **C)** PAR overlay assay of CoV macrodomains. 60 pmoles of macrodomain proteins were slot-blotted on a nitrocellulose membrane and probed with 100 nM protein-free DHBB-purified PAR. PAR binding was detected with 10H and 96-10 anti-PAR antibodies. Histone H1 (1 pmole) and DNAse I (60 pmoles) were used as positive and negative PAR binding controls, respectively. Blots were stained with Sypro Ruby as a loading control. The figure is representative of at least three independent experiments.

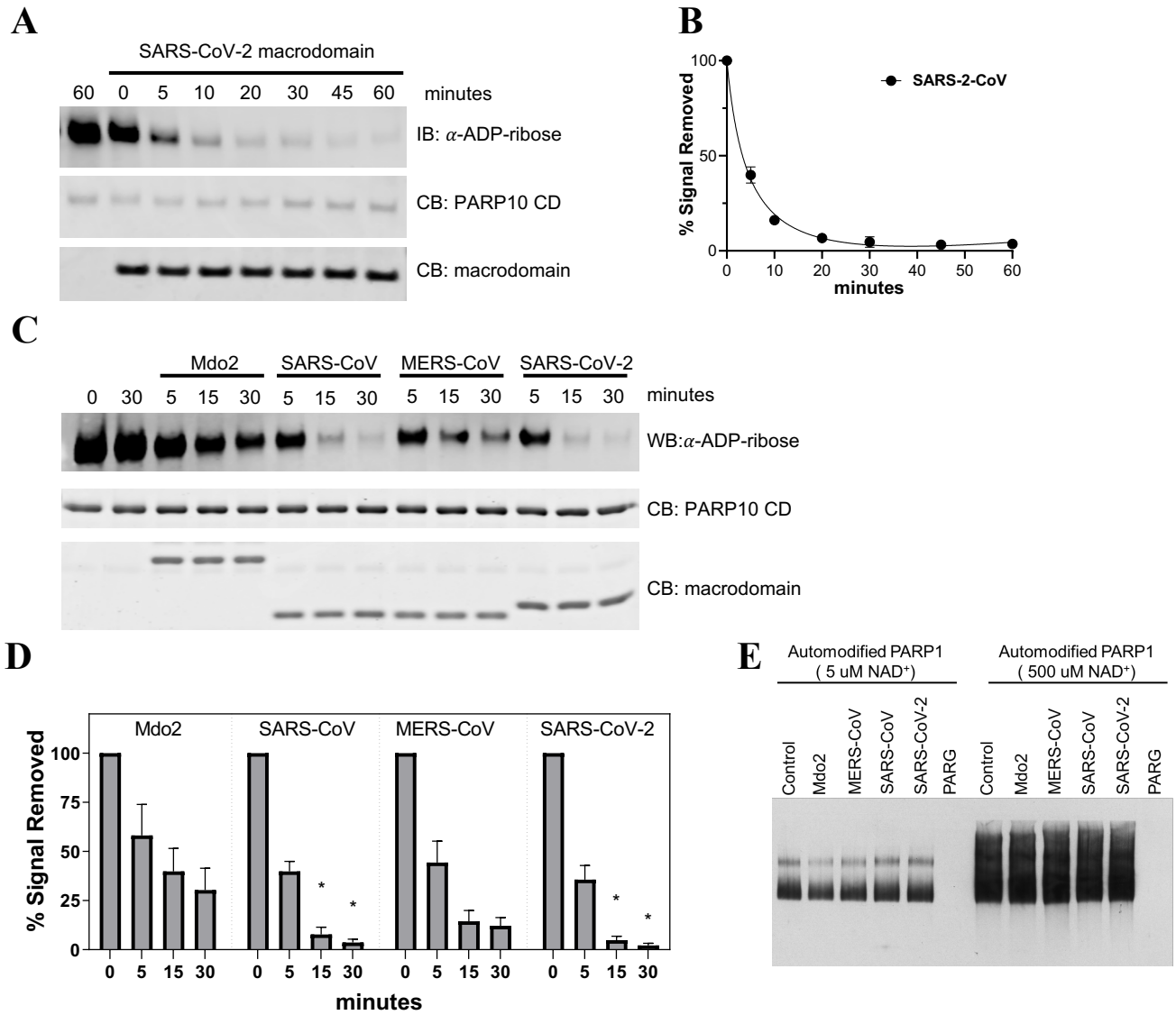


**Figure 6**. SARS-CoV-2, SARS-CoV, and MERS-CoV Mac1 proteins are potent ADP-ribosylhydrolases. **A,C)** The SARS-CoV-2 macrodomain **(A)** or multiple macrodomain proteins **(C)** were incubated with MARylated PARP10 CD *in vitro* for the indicated times at 37°C. ADP-ribosylated PARP10 CD was detected by immunoblot (IB) with anti-ADP-ribose antibody (Millipore-Sigma MAB1076). Total PARP10 CD and macrodomain protein levels were determined by Coomassie Blue (CB) staining. PARP10 CD incubated alone at 37°C was stopped at 0, 30 or 60 minutes. **B,D)** level of de-MARylation was measured by quantifying band intensity using Image J software. Intensity values were plotted and fit to a non-linear regression curve **(B)** or as bar graphs representing the means with error bars representing standard deviation **(D)**. Results in **A** and **C** are representative experiments of two and three independent experiments, respectively. Data in **B** and **D** represent the combined results of two and three independent experiments, respectively. Asterisks indicate statistical significance between these samples and the same timepoint from samples treated with Mdo2. **(E)** PAR hydrolase assays were performed with PARP1 either extensively poly-ADP-ribosylated (500 μM $NAD^+$) or partially poly-ADP-ribosylated (5 μM $NAD^+$) to produce oligo-ADP-ribose. Macrodomains were incubated with both automodified PARP1 substrates for 1 hour. PAR was detected by Western blot with the anti-PAR antibody 96-10. PARG (catalytically active 60 kD fragment) was used as a positive control. The results are representative of at least 2 independent experiments.

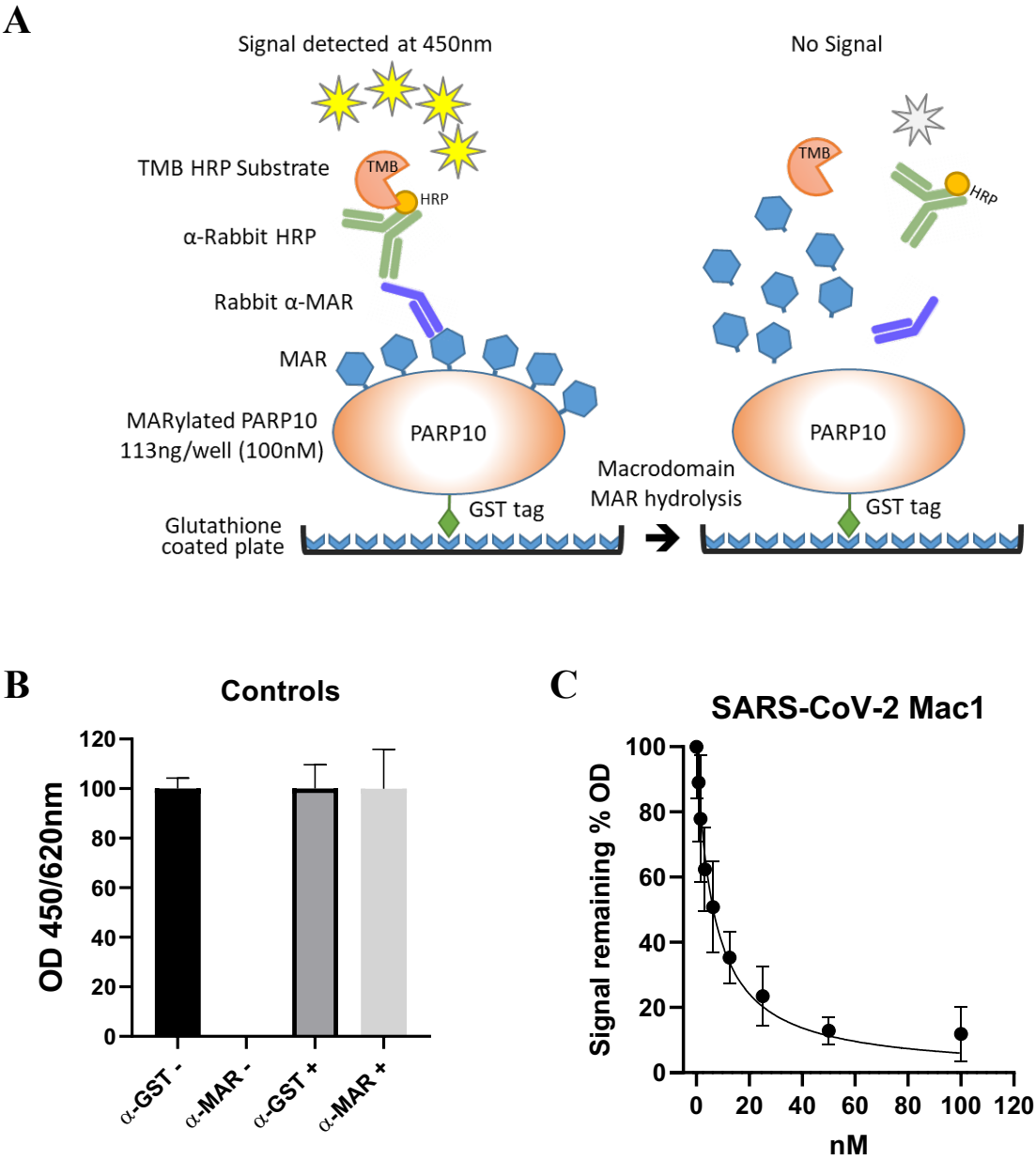


**Figure 7**. Development of an ELISA assay to detect de-MARylation. **A)** Cartoon schematic of the ELISA assay. ELISA plates pre-coated with glutathione and pre-blocked were used capture GST-tagged PARP10 proteins, which was used as a substrate for de-MARylation. The removal of MAR was detected by anti-MAR antibodies. **(B)** MARylated PARP10 (+) and non-MARylated PARP10 (-) with no SARS-CoV-2 Mac1 as controls were detected with anti-mono ADP-ribose antibody α-MAR (Millipore-Sigma MAB1076) or with anti-GST α-GST (Invitrogen, MA4-004). **C)** Starting at 100 nM, 2-fold serial dilutions of the SARS-CoV-2 Mac1 protein was incubated in individual wells with MARylated PARP10-CD for 30 min. at 37°C**.** The graph represents the combined results of 3 independent experiments.